Geological constraints on fluid flow at Whakaari volcano (White Island)

A thesis submitted in partial fulfilment of the requirements for the degree of

Master of Science in Geology

by

Mark J. Letham-Brake

Natural Hazards Research Group

Department of Geological Sciences/Centre for Risk, Resilience, & Renewal

UNIVERSITY OF CANTERBURY
Te Whare Wānanga o Waitaha

October 2013

Frontispiece – Twilight at field camp inside Whakaari's main crater in June 2012.

Table of Contents

Acknowledgements

I extend grateful thanks to: my supervisory team (Dr Ben Kennedy, Dr Elisabeth Bowman, Dr Bettina Scheu, Dr Arthur Jolly, and Dr Michael Heap); University of Canterbury (UC) staff & students (Allison Roberts, Chris Grimshaw, Siale Faitotonu, Sacha Baldwin-Cunningham, Vanessa Tappenden, Cathy Higgins, Simon Bloomberg, James Cowlyn, Noel Win, Jo Pawson, Matt Hanson, Muhamad Yusa, Rebecca Ryder, and Merrick Taylor); Ludwig-Maximilians Universität München (LMU Munich) staff and students (Prof Yan Lavallée [now University of Liverpool], Dr Ulrich Küppers, Klaus Mayer, and Fabian Wadsworth); University of Strasbourg (UniStra) staff (Dr Thierry Reuschlé and Prof Patrick Baud); and GNS Science staff (Dr Gill Jolly, Dr Agnes Mazot, Dr Nico Fournier, Brad Scott, Lauriane Chardot, and Fiona Atkinson). Funding for this project came from the University of Canterbury Mason Trust, a Royal Society of New Zealand Marsden Fund, and an extension of a German Academic Exchange Service (DAAD) Scholarship. Field access was provided by the Buttle Family, Pee Jay Tours, and NZRAF. Historical photograph and publication permissions were provided by GNS Science (Brad Scott) and Whakatane District Museum (Rohi Kaimarama). Sample classification was completed at UC, LMU Munich, and UniStra. Permeability experiments were conducted at UniStra. Special thanks to Simon Bloomberg for introducing me to the field area; Dr Bettina Scheu and Dr Ulrich Küppers for inviting me to Bavaria and Sicily; Dr Nico Fournier, Fabian Wadsworth, and Dr Michael Heap for hosting me during my travels; Prof Jim Cole for your treasure trove of volcanological literature; and the entire GeoNet project team for all you do for the NZ public. Last but by no means least, a massive (!) shout out to my family, flatmates, and friends not already listed, I love you all heaps and appreciated your huge support during this adventure.

Volcano nomenclature

In 1779, Captain James Cook charted ‘White Island,’ but failed to recognise it was a volcano (Wharton, 1893; cited in Hamilton & Baumgart, 1959). The volcano has subsequently been referred to as ‘White Island’ (e.g. Houghton & Nairn, 1989a). However, ‘Te Puia o Whakaari’ was the volcano’s original Māori name as recorded in oral legends (Hochstetter, 1867; cited in Hamilton & Baumgart, 1959) and in early European historic records together with the alias ‘White or Sulphur Island’ (e.g. Fig. A). Conventionally, most New Zealand volcanoes are referred to by their Māori names (e.g. Ruapehu volcano, Ngauruhoe volcano, Tongariro Volcanic Centre, Tarawera volcano, Taupo Volcanic Centre, and Okataina Volcanic Centre), and thus, this study primarily refers to the volcano in question as ‘Whakaari.’

Figure A – Early (c. 1839) sketch of Whakaari labelled as ‘Te Puia o Wakari’ (‘Te Puia o Whakaari’) and ‘White or Sulphur Island.’ Credit: Brad Scott (original artist unknown).

List of Tables

List of Figures

Thesis Abstract

This study assesses the geological constraints on fluid flow within the main crater of Whakaari volcano (White Island) which is located in the Bay of Plenty, New Zealand. A review of the volcanological and morphological history, field mapping, and permeability experiments were used to propose a model for single-state (gas or liquid water) fluid flow in the volcano. Three structural scales were of most importance: (a) the elongate main crater (1.2 km by 0.5 km); which contains (b) three subcraters (~300-500 m in diameter); and (c) >14 historic eruption craters and crater complexes (30-300 m in diameter).

A large ($2.1x10^8$ m^3) sector collapse formed the basic morphology and structure of the amphitheatre-like main crater ≤3.4 ka. Hot fluids are released from magma at ~1–2 km depth and circulated within a conduit-hosted volcano-hydrothermal system. The collapse event was likely to have removed low permeability cone lavas, significantly increasing meteoric water collection and lateral seawater infiltration within high permeability main crater fill above the magma conduit. It is proposed that this caused a susceptibility to 'wet' (i.e. phreatic and phreatomagmatic) eruptions which possibly formed three prehistoric subcraters and has been demonstrated in the last ~200 years of available historic record. The permeability of the remaining in-situ cone lavas is controlled by micro- (<1 mm) and macro- (>1 mm) cracks but despite these cracks, the cone lavas' permeability is still sufficiently low to focus rising magmatic fluid flow through main crater fill. Low-to-high permeability lithified tuffs are inferred to fill the main crater at depth. Low permeability fine ash tuffs generally restrict vertical fluid flow put permit it when vertical trains of vesicles are present. Atmospheric steam and gas pluming is accommodated by a permeable zone of repeated and overlapping historic eruption crater-related discontinuities that extend to >250 m depth through highly

permeable unlithified main crater fill in the west. It is likely to be this material into which the seawater infiltrates from the east. Throughout the main crater, fluid flow is focussed at subcrater margins due to steeply-dipping discontinuities between low permeability lava and low-to-high permeability crater fill deposits. The variable permeabilities of crater fill deposits are due to age-related factors of hydrothermal alteration, reworking/sorting, consolidation, and pore mineralisation. At shallow levels (<100 m depth), vertical fluid flow is diverted to historic eruption crater margins by very low permeability clay (reworked and altered tephra). High permeability coarse ash tuffs, Fe-rich lapilli tuffs, and surficial solfatara deposits do not appear to have much effect on the overall fluid flow system.

The results of this study show that, within active volcanic craters, the spatial distributions of variably permeable lithologies are often related to discontinuous cratering structures. Together, these are significant geological constraints on fluid flow. Morphological changes to crater structure can directly impact the groundwater regime above the magma conduit and may strongly influence the occurrence of wet versus dry eruptions. This process is possibly a significant control on eruptive behaviour at volcanoes with similar fluid flow systems worldwide.

1.0 Introduction

Whakaari (White Island) is an active volcanic island and one of New Zealand's most active volcanoes (Fig. 1). A total of 32 small (VEI 1-3) phreatic, phreatomagmatic, and rare magmatic eruptions have been recorded at Whakaari since 1826 (Table 1). Located within the subduction-related Taupo Volcanic Zone, Whakaari features two predominantly andesitic stratocones that are comprised of lava flows, tuffs, and tephras (Cole et al, 2000). The active Central Cone contains a prehistoric main crater (Fig. 1), with a morphology that has been attributed to sector collapse (Moon et al, 2009) and is divided into three prehistoric subcraters (Fig. 12). Within the western subcrater and the western portion of the central subcrater (i.e. the western half of the main crater), >14 historic eruption craters have been recorded (Fig. 6). Volcanological observations of eruption cratering and seismicity measurements have indicated that unlithified main crater infill deposits extend to >250 m depth (Nairn & Houghton, 1989; Jolly et al, 2012). Exploration drilling to further understand the subsurface geology of Whakaari's main crater has previously been proposed (Wood, 1994) but the drilling program was subsequently abandoned.

Structural complexities, hazardous environments and evolving morphologies make mapping and modelling fluid flow within a volcano's crater a considerable challenge to volcanologists, with flow occurring both diffusely through porous soil and rock, and rapidly, focussed through magmatic and hydrothermal vents (Delmelle & Stix, 2000; Goff & Janik, 2000). The bulk of Whakaari's vertical gas and steam emission occurs through the western subcrater (Fig. 1), but there are fumaroles and hot springs across the whole of the main crater (Fig. 11) and diffuse degassing zones focussed at subcrater margins (Fig. 30). Additionally, Whakaari's main crater has seen semi-continuous development of crater lakes (Fig. 11A) and

was earlier thought to be chemically isolated from the sea (Giggenbach, 1987). However, recent isotopic research provided evidence that seawater does in fact laterally infiltrate this system (Giggenbach et al, 2003; Bloomberg, 2012). Recorded at intervals between November 1983 and August 2006, models of airborne correlation spectrometry (COSPEC) data combined with gas chemistry have indicated long term emissions of ~8500 t d^{-1} H_2O, ~950 t d^{-1} CO_2, and ~400 t d^{-1} SO_2, with minor emissions of other species including H_2S and HCl (Rose et al, 1986; Wardell et al, 2001; Werner et al, 2008). This chemical signature is typical of active volcanism with a high gas input from subducting marine sediments (Giggenbach, 1995).

This study models the geological constraints on single-state (gas or liquid water) fluid flow within Whakaari's relatively accessible main crater (Fig. 1), with new field volcanological data combined with experimentally determined porosity and permeability data. Fluid flow was defined as: (a) hydrothermal fluid flow and circulation, (b) seawater infiltration, and (c) meteoric water collection. Porosity and permeability were important for this study because the permeability of volcanic rocks generally increases with a power-law relation to connected (open) porosity (Klug and Cashman, 1996; Saar and Manga, 1999; Mueller et al, 2005; Mueller et al, 2008). The primary objectives of this study's research plan were to: (a) review Whakaari's volcanological and morphological history (Table 1); (b) map the spatial extent of key geological units, structures, and hydrothermal features within Whakaari's main crater (Fig. 12); (c) measure the connected porosity and intrinsic gas permeability of representative small-scale samples (20 x 40 mm) (Table 2); (d) derive the approximate hydraulic conductivity of these samples (Table 2) and (e) integrate these data into a schematic model explaining the relationships between Whakaari's main crater structure, morphology, lithology, and fluid flow (Fig. 32).

Figure 1 – W oriented aerial photograph of Whakaari volcano in November 2011. Central Cone's main crater occupies the centre of the image. A steam and gas plume rises from the western main crater, demonstrating the high vertical fluid flow from that area. Seawater discolouration (foreground) demarks an acid stream outlet at Crater Bay (centre left), demonstrating the lateral flow of acid brines across the surface of the main crater floor. Pale yellow surficial solfatara deposits have formed on the main crater floor and lower crater walls. Volckner Rocks (background right) suggest a larger edifice existed in prehistoric times. Credit: Ben Kennedy.

Table 1 – Volcanological and morphological history of Whakaari. Bracketed codes under 'Type of activity' (e.g. E21) correspond to eruption units identified in the stratigraphy by Cole et al, 2000.

Date	Type of activity	VEI	Volume (m3)	Origin of activity	Eruption crater volume (m3)	References
<150 ka	Submarine volcanism commences with possible subaerial activity, erosion, and sector collapse(s)	-	-	-	-	Hamilton & Baumgart, 1959; Cole et al, 2000; Scott & Rosenburg, 2007
~22 ka (±0.5 ka)	Magmatic lava flow-producing eruption (E21)	~3	<1.0x10^8	Ngatoro Cone	-	Cole et al, 2000
~21 ka (±0.5 ka)	Magmatic lava flow-producing eruption (E20)	~3	<1.0x10^8	Ngatoro Cone	-	Cole et al, 2000
~20 ka (±0.5 ka)	Magmatic lava flow-producing eruption (E19)	~3	<1.0x10^8	Ngatoro Cone	-	Cole et al, 2000
~19 ka (±0.5 ka)	Magmatic lava flow-producing eruption (E18)	~3	<1.0x10^8	Ngatoro Cone	-	Cole et al, 2000
~18 ka (±0.5 ka)	Magmatic lava flow-producing eruption (E17)	~3	<1.0x10^8	Ngatoro Cone	-	Cole et al, 2000
~17 ka (±0.5 ka)	Magmatic lava flow-producing eruption (E16)	~3	<1.0x10^8	Ngatoro Cone	-	Cole et al, 2000
~16 ka (±0.5 ka)	Magmatic lava flow-producing eruption (E15)	~3	<1.0x10^8	Ngatoro Cone	-	Cole et al, 2000
~15 ka (±0.5 ka)	Magmatic lava flow-producing eruption (E14)	~3	<1.0x10^8	Ngatoro Cone	-	Cole et al, 2000
~14 ka (±0.5 ka)	Magmatic lava flow-producing eruption (E13), possibly associated with tephra eruption	~3	<1.0x10^8	Ngatoro Cone	-	Cole et al, 2000
~13 ka (±0.5 ka)	Magmatic lava flow-producing eruption (E12)	~3	<1.0x10^8	Ngatoro Cone	-	Cole et al, 2000
~12 ka (±0.5 ka)	Magmatic lava flow-producing eruption (E11), possibly associated with tephra eruption	~3	<1.0x10^8	Ngatoro Cone	-	Cole et al, 2000
~11 ka (±0.5 ka)	Magmatic lava flow-producing eruption (E10), possibly associated with tephra eruption	~3	<1.0x10^8	Central Cone	-	Cole et al, 2000

~10 ka (±0.5 ka)	Magmatic lava flow-producing eruption (E9)	~3	<1.0x10^8	Central Cone	-	Cole et al, 2000
>10 ka	Hydrothermal circulation commences	-	-	Central Cone	-	Giggenbach & Glasby, 1977; Giggenbach et al, 2003
~9 ka (±0.5 ka)	Magmatic lava flow-producing eruption (E8)	~3	<1.0x10^8	Central Cone	-	Cole et al, 2000
~8 ka (±0.5 ka)	Magmatic lava flow-producing eruption (E7)	~3	<1.0x10^8	Central Cone	-	Cole et al, 2000
~7 ka (±0.5 ka)	Magmatic lava flow-producing eruption (E6)	~3	<1.0x10^8	Central Cone	-	Cole et al, 2000
>6 ka (±0.5 ka)	Magmatic lava flow-producing eruption (E5)	~3	<1.0x10^8	Central Cone	-	Cole et al, 2000
between 3.4 – 2.6 ka	Magmatic lava flow, tephra, and welded airfall-producing eruption (E4)	~3	<1.0x10^8	Central Cone	-	Cole et al, 2000
between 3.4 – 2.6 ka	Magmatic lava flow-producing eruption (E3)	~3	<1.0x10^8	Central Cone	-	Cole et al, 2000
≤3.4 ka	Sector collapse forms main crater; eruption(s) possible	-	2.1x10^8	Central Cone	-	Cole et al, 2000; Moon et al, 2009
≤3.4 ka	Subcraters form, continuous or semi-continuous eruptions	-	-	Main crater	-	Cole et al, 2000
1 Dec. 1826	Phreatic tephra eruption	2	5.0x10^6	Main crater	5.3x10^4	Williams, 1826; cited in Hamilton & Baumgart, 1959; Smithsonian Institution, 2013
1836 (± 2 y)	Phreatomagmatic tephra eruption	2	5.0x10^6	Main crater	5.3x10^4	Polack, 1838; cited in Hamilton & Baumgart, 1959; Smithsonian Institution, 2013
Oct. 1885	Phreatic tephra eruption	2	5.0x10^6	Main crater	5.3x10^4	NZ Herald, 1885; cited in Hamilton & Baumgart, 1959; Smithsonian Institution, 2013
16 Sep. - Dec. 1886	Phreatomagmatic tephra eruption	2	5.0x10^6	W end of main crater	5.3x10^4	Smith, 1887; cited in Hamilton & Baumgart, 1959; Smithsonian Institution, 2013
13 May 1909	Phreatic tephra eruption	2	5.0x10^6	Main crater	5.3x10^4	NZ Herald, 1909; cited in Hamilton & Baumgart, 1959; Smithsonian Institution, 2013

1913	Drainage of crater lake	-	-	Central & eastern subcrater	-	Hamilton & Baumgart, 1959
10 Sep. 1914	Sector collapse	-	2.5x10^5	SW wall of main crater	-	Ward, 1922 & Bartrum, 1926; cited in Hamilton & Baumgart, 1959; Smithsonian Institution, 2013
Dec. 1922	Phreatic tephra eruption	2	5.0x10^6	NW end of main crater	5.3x10^4	Evening Post, 1923 & Auckland Weekly News, 1923; cited in Hamilton & Baumgart, 1959; Smithsonian Institution, 2013
Sep. 1924	Phreatic tephra eruption	2	5.0x10^6	NW end of main crater	5.3x10^4	Evening Post, 1924 cited in Hamilton & Baumgart, 1959; Smithsonian Institution, 2013
3 Feb. 1926	Phreatic tephra eruption	2	5.0x10^6	SW end of main crater	5.3x10^4	Grange, 1927; cited in Hamilton & Baumgart, 1959; Smithsonian Institution, 2013
1 - 3 Sep. 1928 (±1 d)	Phreatic tephra eruption	1	5.0x10^5	W end of main crater	1.0x10^5	NZ Herald, 1928; cited in Hamilton & Baumgart, 1959; Smithsonian Institution, 2013
2 Apr. 1933	Phreatic tephra eruption	3	5.0x10^7	1933 Crater	2.65E+05	Goosman, 1933; cited in Hamilton & Baumgart, 1959; Smithsonian Institution, 2013
before Jan. 1947	Phreatic tephra eruption	2	5.0x10^6	Noisy Nellie	5.3x10^4	Cole & Nairn, 1975; Smithsonian Institution, 2013
Jan. 1955	Phreatic tephra eruption	2	5.0x10^6	Noisy Nellie	5.3x10^4	Cole & Nairn, 1975; Smithsonian Institution, 2013
11 Dec. 1957	Phreatic tephra eruption	2	5.0x10^6	Noisy Nellie	5.3x10^4	Cole & Nairn, 1975; Smithsonian Institution, 2013
Dec. 1958	Phreatic tephra eruption	1	5.0x10^5	Noisy Nellie & 1933 Crater	1.0x10^5	Cole & Nairn, 1975; Smithsonian Institution, 2013
14 - 20 Dec. 1959	Phreatic tephra eruption	2	5.0x10^6	Noisy Nellie	5.3x10^4	Cole & Nairn, 1975; Smithsonian Institution, 2013
15 Dec. 1962	Phreatic tephra eruption	3	5.0x10^7	Big John	1.0x10^6	Cole & Nairn, 1975; Smithsonian Institution, 2013
13 Nov. 1966 - Mar. 1967	Phreatic tephra eruption	3	5.0x10^7	Gilliver	3.39E+05	Cole & Nairn, 1975; Smithsonian Institution, 2013

27 Jan. 1968 - Feb. 1969	Phreatic tephra eruption	3	5.0x10^7	Rudolf	1.91E+05	Cole & Nairn, 1975; Smithsonian Institution, 2013
Aug. - Sep. 1969	Phreatic tephra eruption	2	5.0x10^6	Rudolf	5.3x10^4	Cole & Nairn, 1975; Smithsonian Institution, 2013
Jun. 30 1970 (±30 d)	Phreatic tephra eruption	2	5.0x10^6	Rudolf	5.3x10^4	Cole & Nairn, 1975; Smithsonian Institution, 2013
9 Apr. 1971 (± 3 d)	Phreatic tephra eruption	2	5.0x10^6	Noisy Nellie	5.3x10^4	Cole & Nairn, 1975; Smithsonian Institution, 2013
19 - 20 Jul. 1971	Phreatic tephra eruption	2	5.0x10^6	1971 Crater	5.3x10^4	Cole & Nairn, 1975; Smithsonian Institution, 2013
8 Sep. 1974 (± 10 d)	Phreatic tephra eruption	2	5.0x10^6	1971 Crater	5.3x10^4	Clark & Cole, 1976 cited in Clark & Cole, 1989; Smithsonian Institution, 2013
18 Dec. 1976 - 29 Jan. 1982	Phreatic, phreatomagmatic, & strombolian tephra eruption (3 phases) (E2 & E1)	3	1.0x10^7	1978 Crater Complex	<1.0x10^7	Houghton & Nairn, 1989a; Houghton & Nairn, 1991; Smithsonian Institution, 2013
26 Dec. 1983 (±5 d) - 12 Feb. 1984 (± 5 d)	Phreatic tephra eruption	2	5.0x10^6	N margin of 1978 Crater Complex	5.3x10^4	Houghton & Nairn, 1989a; Houghton & Nairn, 1991; Smithsonian Institution, 2013
1 Feb. 1986 - 28 Jul. 1994	Phreatic and phreatomagmatic tephra eruption	3	5.0x10^7	Donald Duck, 1978 Crater Complex, & TV1	1.0x10^6	IGNS,1986-1994; Smithsonian Institution, 2013
28 - 29 Jun. 1995	Phreatic tephra eruption	1	5.0x10^5	Wade & Princess	1.0x10^5	IGNS, 1995; Smithsonian Institution, 2013
28 - 29 Mar. 1998	Phreatic tephra eruption	1	5.0x10^5	NW margin of 1978 Crater Complex	1.0x10^5	IGNS, 1998; Smithsonian Institution, 2013
22 Aug. 1998 - Aug. 1999	Phreatomagmatic tephra eruption	2	5.0x10^6	Metra & PeeJay	5.3x10^4	IGNS, 1998-99; Smithsonian Institution, 2013
7 Mar. 2000 - 5 Sep. 2000 (± 4 d)	Phreatomagmatic tephra eruption	3	5.0x10^7	MH	2.65E+05	IGNS, 2000; Smithsonian Institution, 2013
19 Feb. 2001	Phreatic tephra eruption	2	5.0x10^6	MH	5.3x10^4	GeoNet, 2001; Smithsonian Institution, 2013
5 Aug. 2012 – 2013 (presently active)	Phreatic and phreatomagmatic tuff-cone forming tephra & magmatic dome-forming eruption	1	5.0x10^5	2012 Tuff Cone & "The Gremlin" at site of Sulphur Crater	-	GeoNet, 2012-13

2.0 Geological setting

2.1 Regional setting

Whakaari lies in New Zealand's Taupo Volcanic Zone (TVZ) (Fig. 2 inset, Fig. 3), which is a result of subduction of the Pacific Plate westward below the Australian Plate (Fig. 3) and demarks the southern terminus of the Tonga–Kermadec volcanic arc (Wright, 1992; Cole et al, 2000). Whakaari is an offshore volcanic island located on the continental shelf, 48 km north of the town of Whakatane on the Bay of Plenty coastline (Fig. 2) and 200 km west of the subduction interface associated with the TVZ (Hikurangi Trench) (Fig. 3). Over the last 20 ka, NW-SE extension across the NE-SW oriented Whakatane Graben, within which Whakaari is located (Fig. 2), has occurred at a rate of 12.6 ± 3.5 mm yr^{-1} (Lamarche et al, 2006). Mafic magmas generated by dehydration of the Pacific Plate slab in the mantle wedge below Whakaari (Fig. 3) rise through the continental crust of the Australian Plate, mix, and fractionate to produce intermediate cone-building lavas composed of andesite, dacite, and basaltic andesite in decreasing frequency, with phenocryst contents ranging from 15 to 44 % (Cole, 1990; Cole et al, 2000). Andesitic volcanism associated with rifting within the modern TVZ commenced ~1.9-2.0 Ma (Eastwood et al, in prep.; Wilson et al, 1995). However, Whakaari's volcanism has been suggested to have commenced only 150 ka (Scott & Rosenberg, 2007).

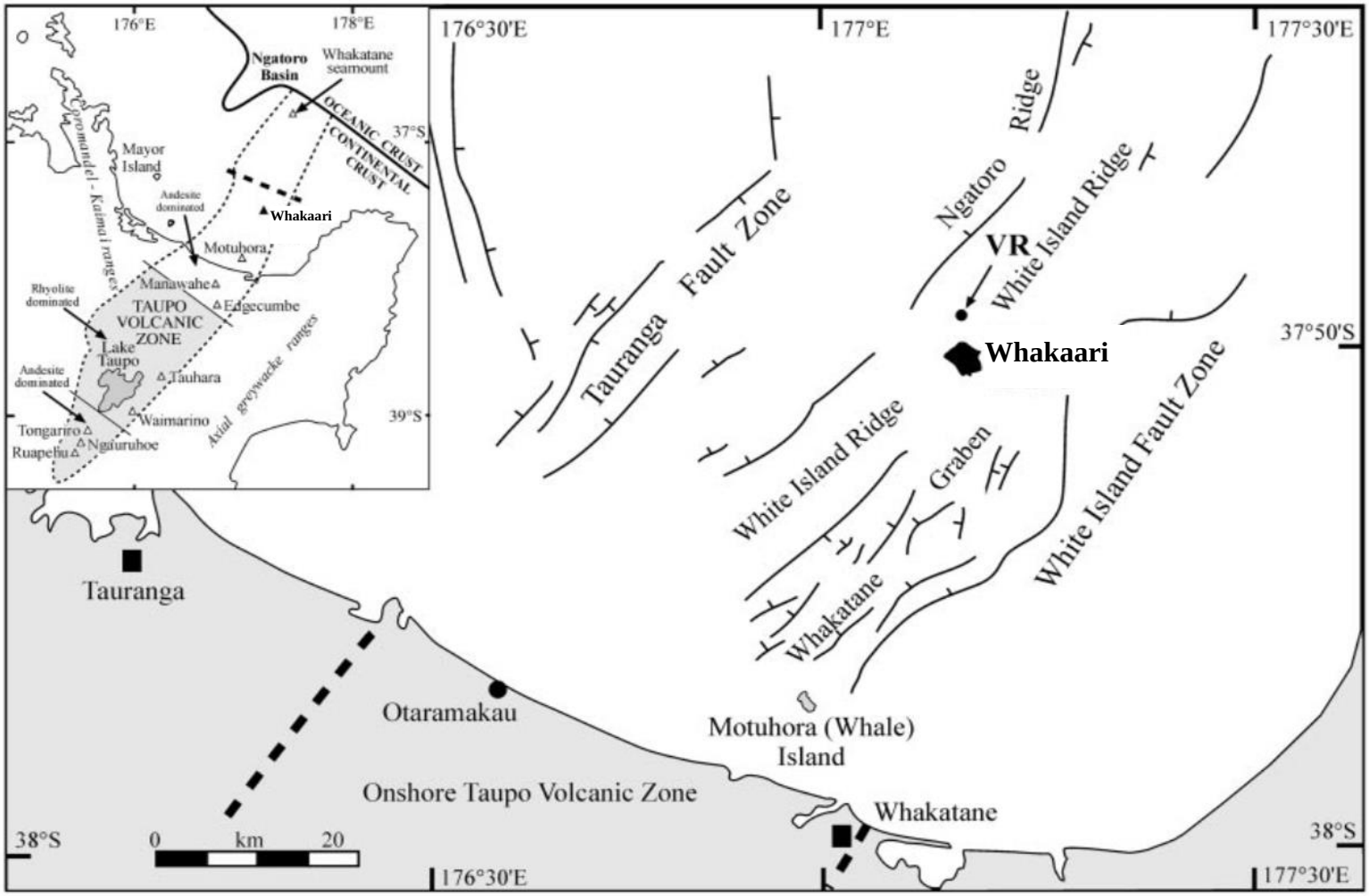

Figure 2 – Structural map of Whakaari's regional setting. Showing extensional structural elements (after Wright, 1992) and Whakaari's regional setting in the Bay of Plenty (modified from Cole et al, 2000). Inset map shows Whakaari's regional setting within the Taupo Volcanic Zone.

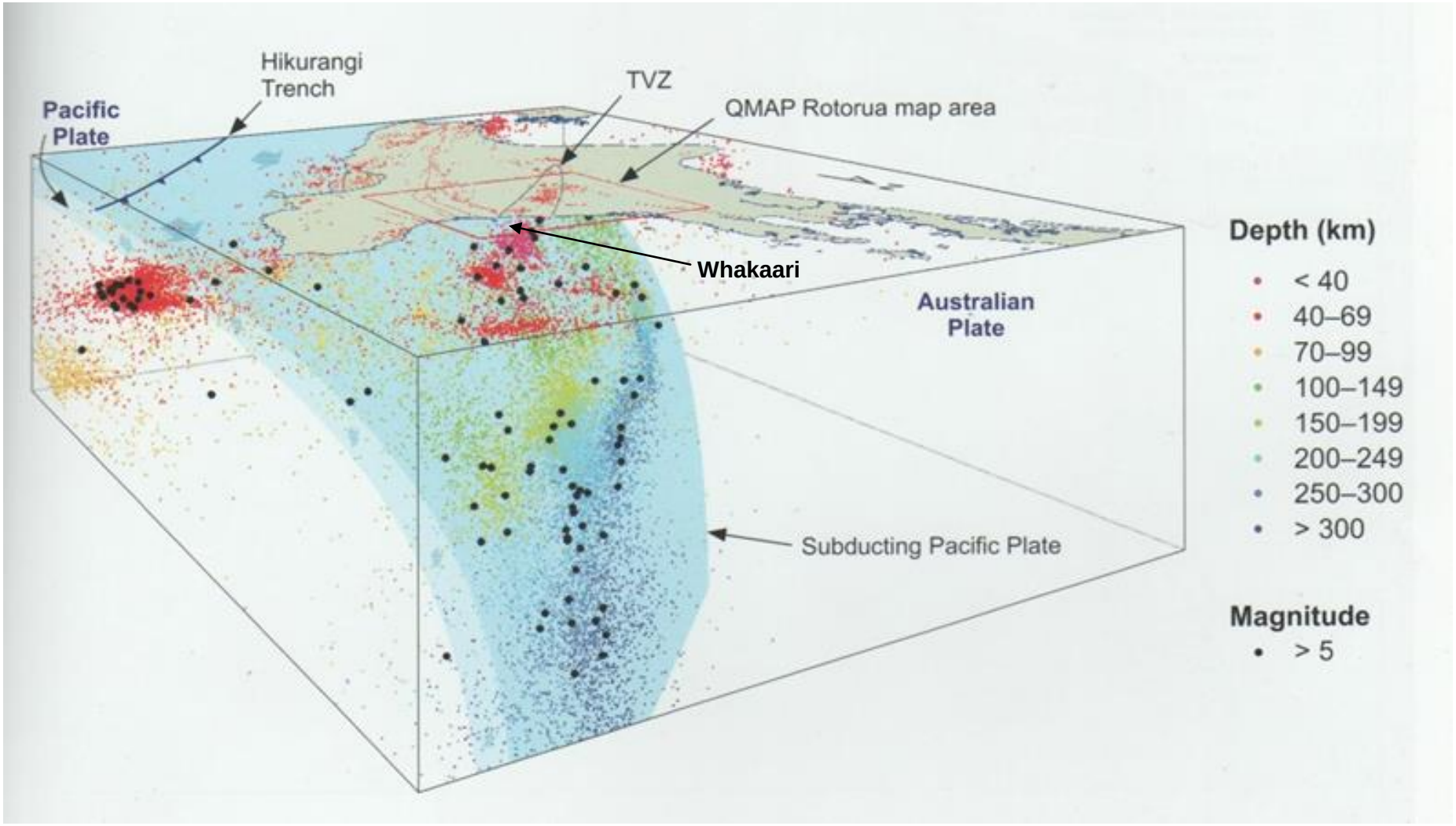

Figure 3 – SW oriented 3D seismic model of Whakaari's tectonic setting at the Australian-Pacific plate boundary. Historical earthquake epicentres are split into two populations. Earthquakes >M5 (M = Richter magnitude) are depicted as black circles; all recorded earthquakes during the period of 1990-2009 between M5 and M2 are depicted as points, colour-ramped by depth. This pattern of seismicity defines the curved, west-dipping, subducting slab of the Pacific Plate. The over-riding Australian Plate thins beneath the TVZ (due to back-arc rifting), but this is not shown for simplicity. The surface location of Whakaari is labelled. Modified from Leonard et al, 2010.

2.2 Volcanological and morphological history

Māori legends indicate that volcanic and hydrothermal activity was present at Whakaari prior to European settlement of New Zealand (Hochstetter, 1867; cited in Hamilton & Baumgart, 1959). In 1779, Captain James Cook charted 'White Island,' but failed to recognise it was a volcano (Wharton, 1893; cited in Hamilton & Baumgart, 1959). At intervals between 1885 and 1934, a total of ~10^3 short tons (9.07 x 10^6 kg) of sulphur were mined from Whakaari's main crater (Hamilton & Baumgart, 1959). In October 1885, a ballistic block eruption prompted miners to evacuate (NZ Herald, 1885; cited in Hamilton & Baumgart, 1959). Later, on 10th September 1914, a collapse of the SW crater wall triggered a debris avalanche which killed 11 miners (Ward, 1922, & Bartrum, 1926; cited in Hamilton & Baumgart, 1959). There have been no reported casualties since 1914 and Whakaari is now an uninhabited private reserve, however ballistic tephra eruptions and failure(s) of the inner crater walls remain potential hazards to the >13,500 annual visitors (Nairn et al, 1996; Moon et al, 2009; visitor numbers: Pee Jay Tours Ltd, pers. comm., 2012). Recent volcanic activity has consisted of small phreatic, phreatomagmatic, and rare magmatic events, with the most recent heightened period of unrest presently on-going since August 2012 (GeoNet, 2012-13).

Whakaari's volcanological and morphological history (Table 1) was the basis for this study's discussion of how the modern fluid flow system was formed (Section 6). Here, each 'eruption' was defined as a period of heightened unrest in which one or more directly associable explosive eruptive events were recorded. This becomes problematic when determining the Volcanic Explosivity Index (VEI, after Newhall & Self, 1982) because discrete explosions at Whakaari are historically "small" and "weak" (Houghton & Nairn, 1991). However, this eruption definition was also applied by the Smithsonian Institution

(2013), who prescribed Volcanic Explosivity Index values for most of Whakaari's eruptions. Thus, this definition is applied in this study to at least give a broad comparison of the volcano's explosivity (Fig. 5). The dates, types (i.e. magmatic, phreatomagmatic, or phreatic eruption, sector collapse, etc.), and origins of activity were collated, inferred, or interpreted in this study from historic sources (Hamilton & Baumgart, 1959; Cole & Nairn, 1975; Clark & Cole, 1989; Houghton & Nairn, 1989b; IGNS, 1986-2001; & GeoNet, 2001-13), and stratigraphic (Cole et al, 2000) and radiometric (Thordarson & Houghton, unpub., 1999, cited in Cole et al, 2000) investigations. The VEI values were those prescribed by the Smithsonian Institution (2013) except for (a) the 2012-13 eruption, in which the VEI value was not prescribed by the Smithsonian Institution and therefore was interpreted in this study from observations by GeoNet (2012-13), and (b) the prehistoric eruptions, in which all were interpreted as VEI ~3 based on the generic lava flow volume given in Cole et al (2000). The eruption volumes presented in this study were estimated using the mean volumes for equivalent VEI events, except for the 1976-1982 eruption in which the volume had been estimated by Houghton & Nairn (1989b) using direct physical volcanological observations. The prehistoric sector collapse volume was identified in the best-fit geomorphic model by Moon et al (2009) and the 1914 sector collapse volume was estimated from descriptions in Hamilton & Baumgart (1959). The eruption crater volumes were collated, averaged, and extrapolated from volumes estimated by Cole & Nairn (1975) and Nairn & Houghton (1989), based on the assumption that eruption crater volumes at Whakaari are directly correlated with the VEI.

There has been an apparent evolution in the eruption style at Whakaari (i.e. the occurrence of wet versus dry eruptions). Although Cole et al (2000) noted that minor tephra and tuff deposits corresponding to additional eruptions may be under-represented due to poor

preservation (i.e. possibly representing wet *or* dry volcanism), 19 known prehistoric eruption units are interpreted as representing magmatic 'dry' eruptions because they emplaced <0.1 km^3 lava flows with a return period of 0.5 to 1.5 ka (Table 1). Interestingly, however, radiometric evidence has showed that no lava flows have been erupted since between 3.4 and 2.6 ka (Thordarson & Houghton, unpub., 1999; cited in Cole et al, 2000). Since 1826, 30 out of 32 recorded eruptions have been of a phreatic or phreatomagmatic 'wet' eruption style (Table 1). The exceptions to this were (a) during the 1976-82 eruption, when three phases of strombolian activity followed three associated phases of vent-clearing phreatic and phreatomagmatic activity (Fig. 4A); and (b) during the 2012-13 eruption, when a small, spiny lava dome was effusively emplaced (Fig. 4B). Whakaari's overall historic susceptibility to wet eruptions (Fig. 4C & 4D) has been attributed to the intrusion of magma into wet main crater infill (Houghton & Nairn, 1991). The explosivity (VEI 3) of one of Whakaari's largest known eruptions, during 1976-82, is small compared to major explosive eruptions that have occurred worldwide (Fig. 5). A potential causal link between Whakaari's morphology, fluid flow, and the apparent evolution from dry to wet eruption style is considered in the discussion (Section 6).

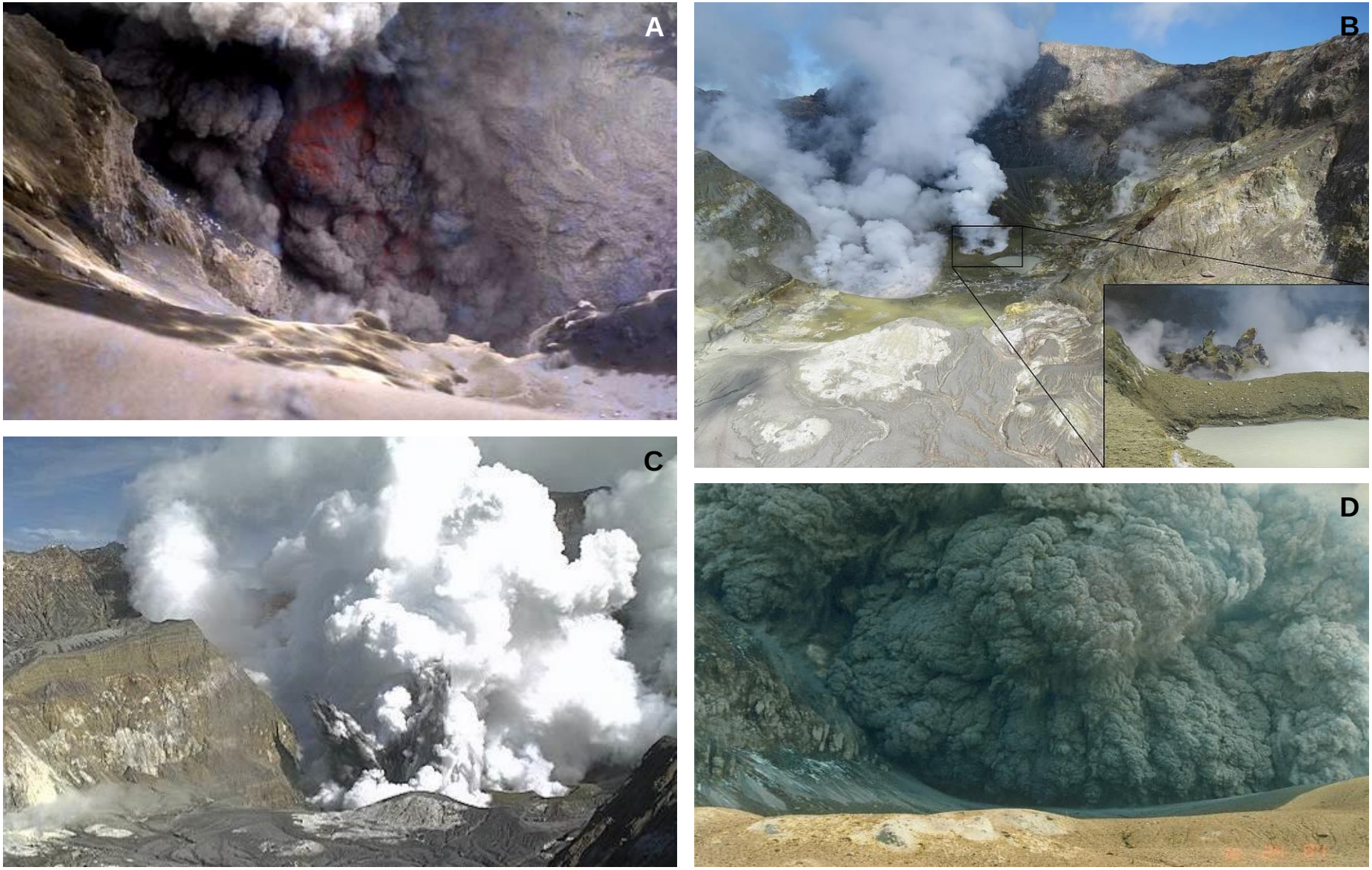

Figure 4 – Photographs of historical styles of volcanism at Whakaari. 4A: N oriented photograph of strombolian activity in Christmas Crater on 4 April 1977 (became 1978 Crater Complex – Fig. 7). Credit: Simon Nathan. 4B: W oriented photograph of "The Gremlin" lava dome on 10 December 2012. 4C: W oriented photograph of phreatic activity in the 1978 Crater Complex on 20 August 2013. Credit: GeoNet. 4D: NW oriented photograph of phreatomagmatic activity in 1978 Crater Complex on 25 March 1988. Credit: Ian Nairn.

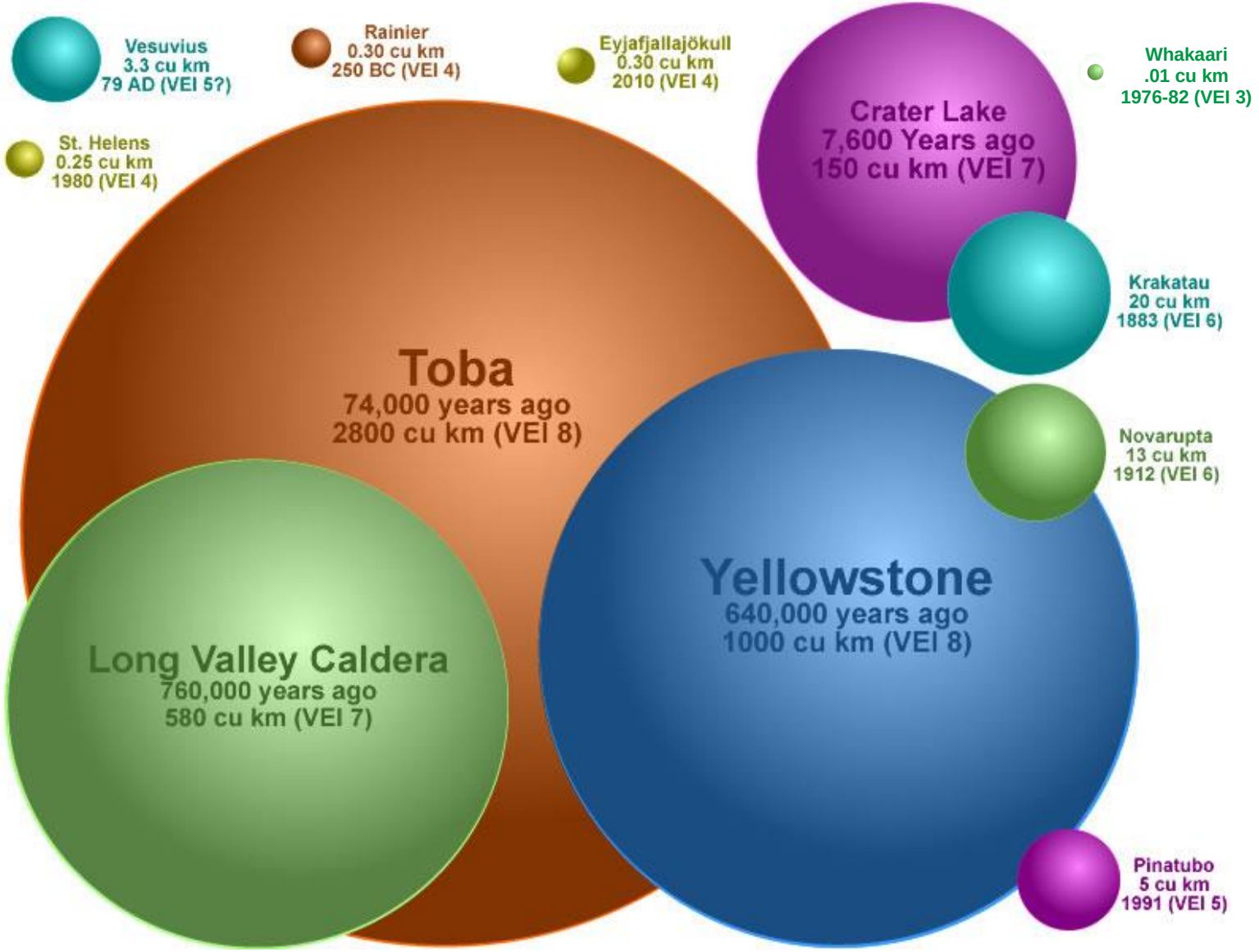

Figure 5 – Schematic diagram comparing the eruption volume and VEI (Volcanic Explosivity Index) of Whakaari's 1976-82 eruption to those of major eruptions worldwide. Modified from King, 2013. Whakaari 1976-82 eruption VEI prescribed by Smithsonian Institution, 2013.

2.3 Structural setting

2.3.1 Cone structure

The 321 m high subaerial structure of Whakaari (Fig. 1) measures 2.4 km east–west by 2 km north–south and represents the summit of a much larger (16 by 18 km) submarine structure that rises 300-400 m from the sea floor (Duncan, 1970; Moon et al, 2009). Outlying subaerial lava sea stacks at Club Rocks and Volckner Rocks (Fig. 1 & 2) suggest that this structure was significantly larger in prehistoric times (Hamilton & Baumgart, 1959; Cole et al, 2000). Whakaari's modern subaerial structure consists of two volcanic cones: an older, extinct, and eroded cone, referred to as Ngatoro Cone, overlapped by a younger, active cone, referred to as Central Cone (Black, 1970; Duncan, 1970; Cole et al, 2000). Both cones are stratocones that are comprised of major lava flow units, and minor tuff and tephra units (Cole and Nairn, 1975; Cole et al, 2000).

2.3.2 Main crater structure

The Central Cone's main crater (Fig. 1), which is the focus of this study (referred to as 'the main crater'), measures 1.2 km NW-SE by 0.5 km NE-SW and is infilled with unlithified deposits (Fig. 1). It is breached by the sea at three locations in the southeast: Crater Bay, Wilson Bay, and Shark Bay (Fig. 1 & 6). Geomorphic modelling of the main crater, together with the detection of large debris fans in bathymetry to the east of the island (Moon et al, 2009), and previously characterised rock strength data (Moon et al, 2005), showed that the amphitheatre-like structure of the modern main crater was formed by a large (2.1×10^8 m^3) prehistoric, eastward-trending sector collapse (Table 1). In this study, the event is considered

one of the most important morphological changes for Whakaari's fluid flow system and its age is inferred in the discussion (Fig. 29). Blocky volcaniclastic deposits from the smaller ($2.5x10^5$ m^3) collapse in 1914 (Table 1) are represented by hummocky topography on the main crater floor, which is otherwise relatively flat but dips southeast ~5° and rises to more than 30 m a.s.l. at Donald's Mound (Fig. 6).

2.3.3 Subcrater structure

Based on three coalescing, circular morphological shapes measuring 300-500 m in diameter within the main crater (Houghton & Nairn, 1989a; Moon et al, 2009), anomalous thermal peaks (Mongillo & Wood, 1995), and CO_2 soil gas flux peaks (Bloomberg, 2012), the main crater is divided into three subcraters (Fig. 30 & 32). Volcanological observations of deep excavation within the 1978 Crater Complex show that unlithified tephra and volcaniclastics fill the western subcrater to a depth of >250 m (Nairn & Houghton, 1989). Low seismic velocities recorded across the main crater by helicopter mass drop experiments between September and November 2011 indicate that unlithified material also extends to a similar depth in the central and western subcraters (Jolly et al, 2012). The results of a high resolution (<2 m) thermal infrared survey completed in April 1992 suggested that "the morphology of the subcraters is of considerable importance because their margins are zones of structural weakness, likely to provide vertical permeability for thermal fluids" (Mongillo & Wood, 1995). This was proven with a medium-to-high resolution (<20-5 m) CO_2 soil gas flux survey completed between November 2010 and November 2011 which showed that diffuse CO_2 degassing pathways are controlled by vertical "fault-related" permeability at the margins of the central and eastern subcraters (Bloomberg, 2012).

2.3.4 Eruption crater structure

Whakaari's historic eruption craters and crater complexes have measured 30-300 m across and have been located within the western portion of the central subcrater and the western subcrater (i.e. the western half of the main crater) (Fig. 6). Complementary to explosive eruption cratering mechanisms observed at other volcanoes (Sottili et al, 2012) and modelled in analogue experiments (Roche et al, 2001), eruption cratering at Whakaari is controlled by subsidence, explosive excavation, and collapse (Fig. 7, 8 & 9). The shallow (0-250 m) zone of overlapping eruption craters within the western subcrater (Fig. 6) accommodates the bulk of Whakaari's continuous vertical gas and steam flow (Houghton & Nairn, 1989a; Werner et al, 2008). All historical eruption craters have become partially (Fig. 18) or completely (Fig. 10) infilled with unlithified deposits, though both the water table and ground surface in the western subcrater have generally lowered due to formation of the 1978 Crater Complex (Hurst et al, 2004). Whakaari's eruption craters may re-activate, and excavate and re-deposit infill material due to subsequent eruptions (Table 1) (Fig. 6).

2.3.5 Conduit structure

Below the main crater floor, a viscous, degassing magma plug accommodating late-stage fractionation is believed to be located at ~1-2 km depth, with a magmatic plumbing system located between ~2-7 km depth (Houghton & Nairn, 1989a; Cole et al, 2000). Based on modelling of COSPEC and fumarole chemistry data collected between 2002 and 2004, the volume of the shallow magma plug was estimated at between 0.015 and 0.04 km^3 (Werner et al, 2008). Eruption observations (Houghton & Nairn, 1989b), deformation modelling (Clark & Otway, 1989), and magnetic surveys (Christoffel, 1989) show that magma advanced by

500 m between 1973 and 1977, reaching <500 m depth, and then retreated 250 m between 1977 and 1980 (Houghton & Nairn, 1989a). This advance and retreat of conduit magma was associated the 1976-82 VEI 3 eruption (Table 1). Simultaneous tephra ejection in Gibrus and Christmas Craters (before they coalesced into the 1978 Crater Complex) (Fig. 9), and their formation on the same sites as the 1933, 1971, and Gilliver Craters (Fig. 6 & 7), suggested that Whakaari's eruption craters may be linked at depth by a relatively stable magma conduit beneath the western subcrater (Houghton & Nairn, 1989a). This hypothesis is strengthened by the fact that most eruptions since 1978, including the presently on-going activity, have also occurred within the 1978 Crater Complex (Fig. 6).

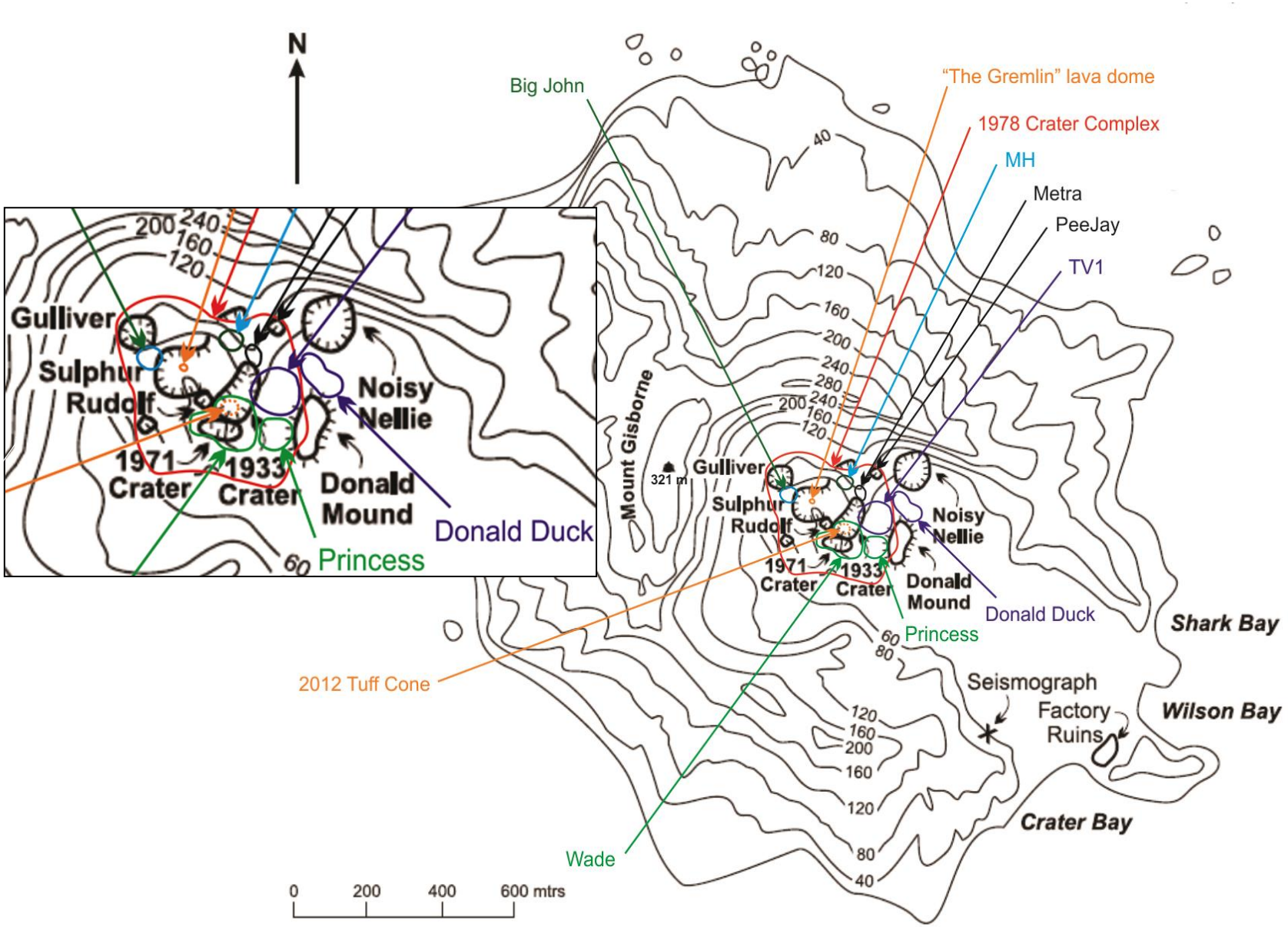

Figure 6 – Topographic map of Whakaari showing the locations of historic eruption craters. Modified from Nairn & Houghton, 1989; Nairn et al, 1996; Hurst et al, 2004; & Scott & Sherburn, 2007.

Figure 7 – NW oriented aerial photograph of Gilliver crater c. late 1966. Note the steeply-dipping crater wall geometry. Credit: Bill Crafar.

Figure 8 – W oriented aerial photograph of explosive excavation in Gibrus crater on 16 March 1978 (became 1978 Crater Complex – Fig. 7). Credit: A.J. Hull.

Figure 9 – W oriented photograph of the 1978 Crater Complex c. late 1978. Note collapse due to slumping (foreground) and a short-lived lake in Christmas Crater (centre). Credit: Lloyd Homer. Volcanologists for scale (upper left).

Figure 10 – SW oriented photograph of infilled Noisy Nellie crater c. late 1971. A clay ‘cap’ diverts diffuse degassing to the crater margins (foreground). Note Donald Mound fumaroles (right background). Credit: Ted Lloyd.

2.4 Hydrothermal setting

Whakaari hosts a hydrothermal system that has been active for >10 ka (Giggenbach & Glasby, 1977; Giggenbach et al, 2003) with fluid flow today expressed at the surface by crater lakes, hot springs, fumaroles, and acid streams (Fig. 11). Geophysical surveillance since 1967 has identified that the main foci of subsurface hydrothermal fluid flow migrate in semi-regular cycles (2-10 yr) (Peltier et al, 2009; Fournier & Chardot, 2012). Such foci have occurred proximal to existing and newly formed eruption craters and 200-650 °C fumarole fields, generally shifting between 100m and <1 depth (Clark & Otway, 1989; Christoffel, 1989; Hurst et al, 2004; Peltier et al, 2009; Fournier & Chardot, 2012). Peltier et al (2009) and Fournier & Chardot (2012) suggested that cyclic periods of ground inflation (≤250 mm) are due to thermal expansion and pore-pressure increases at ~200-600 m depth, reflecting the presence of magma below the central and western subcraters. Nishi et al (1996) concluded, from detailed seismic modelling of shallow (<1 km) earthquakes recorded between January and March 1992, that "high pore pressures promote shear failure beneath the main crater, but this effect is counterbalanced by a reduction in pressures beneath the western half of the area [i.e. where historic eruption craters have formed – Fig. 6]. Stress corrosion and rock matrix dissolution, both accelerated by the low pH of [Whakaari's hydrothermal] fluids, will reduce bulk strength within the volcano-hydrothermal system." Infiltrating seawater and non-isochemical dissolution of volcanic host rock together form acid brines that become heated and rise to the surface in hot springs (Giggenbach et al, 2003). Analysis of Na, Cl, and O isotopes showed that the magmatic gas contribution to hydrothermal fluid circulation is much higher in the western and central subcraters than in the eastern subcrater, where the seawater contribution is higher (Giggenbach et al, 2003; Bloomberg, 2012).

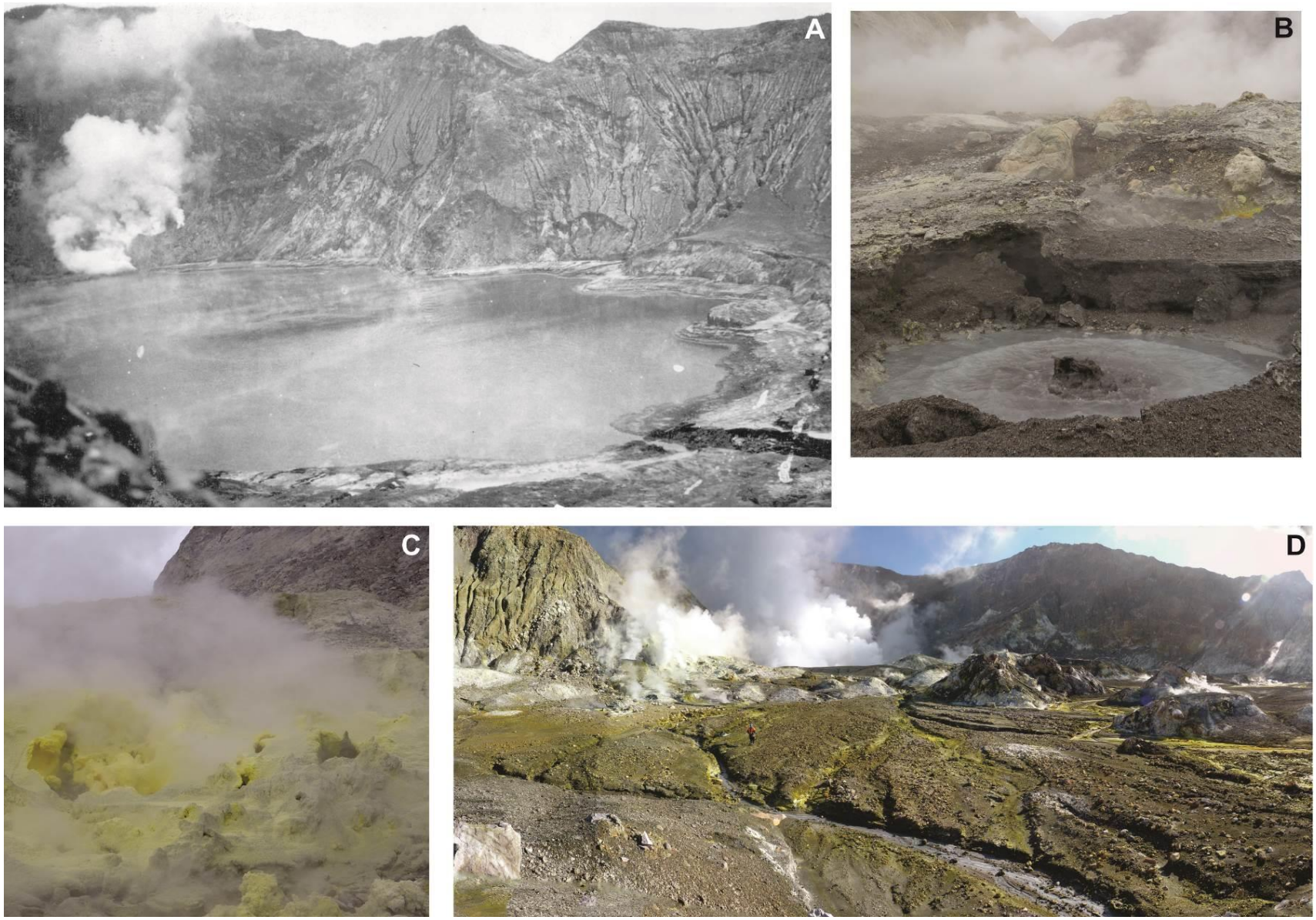

Figure 11 – Photographs of Whakaari's hydrothermal features. A: Crater lake in the central and eastern subcraters prior to artificial drainage in 1913. Credit: Brad Scott (original photographer unknown). B: Hot spring located within the zone of coalescence between the central and eastern subcrater margins in 2012. C: A fumarole field/solfatara in 2013. D: An acid stream bed in 2012. Note rilling of the crater walls (D, left background), steam and gas pluming from the western subcrater lake area (D, centre background), and mounds created by the 1914 collapse debris (D, right background).

3.0 Field mapping and sample classification

3.1 Methods

Whakaari's geological and hydrothermal features were mapped within the main crater during visits in November 2011, June 2012, and June 2013, and remotely with Google Earth satellite imagery. Samples were collected and classified to provide representative lithological constraints on Whakaari's main crater fluid flow with small-scale permeability experiments. The rock samples (lavas, tuffs, and surficial solfatara deposits) were classified by (a) field observations; (b) reflected light microscopy of thin sections; and (c) connected porosity measured by weighing dry, saturated, and submerged samples and applying Archimedes' principle. The unlithified samples (primary and reworked/altered tephras, collected in plastic containers and sealed with plastic tape) were classified by (a) field observations; (c) plasticity index, determined with a cone penetrometer following the New Zealand standard (SANZ, 1986); and (c) connected porosity measured with a Micromeritics 1330 helium pycnometer at Ludwig-Maximilians Universität München (LMU Munich). All field mapping was conducted within the main crater, except for the cone-forming lava flows which were grouped as two units (Ngatoro and Central Cone lava successions; after Cole et al, 2000) based on their spatial extent in exposures in the main crater walls and sea cliffs around the perimeter of the island.

3.2 Results

3.2.1 Field mapping

A geological map of Whakaari is presented in Fig. 12. The locations of fumaroles, hot springs, and acid streams are plotted on a structural map of Whakaari's fluid flow, based on the thermal and mass flux anomalies discovered by Mongillo and Wood (1995) and Bloomberg (2012) (Fig. 30). Annotated field photographs show field relationships (Fig. 13–18).

Discoloured cone lava exposures form steep main crater walls in the north, west, south, and east at Troup Head and Pinnacle Head, but are otherwise absent in the east at Crater, Wilson, and Shark Bays (Fig. 12 & 13). Alternating coarse and fine ash tuffs are inter-bedded with cone lavas and exposed in the south and north main crater walls, in sequences up to 40 m thick (Fig. 12 & 13). At Troup Head, agglomerate is inter-bedded with ash tuffs (Fig. 12). Primary tephra deposits overlie bedded ash tuff on a bench on the southern side of the main crater (South Bench) and are the most abundant deposit exposed on the main crater floor (i.e. deposits are in-situ but likely to have been altered to some extent by diffuse degassing) (Fig. 12 & 16). Surficial solfatara deposits (<20 cm thick) demark active and fossil fumaroles across the main crater floor, on lower main crater walls, and at the margins of Noisy Nellie and Donald Duck eruption craters (Fig. 12, 15, & 17). Lapilli tuffs cemented by iron-rich precipitates are exposed in 5-20 cm–thick stream beds between 20 and 50 m downstream (SE) of a fumarole field at the coalescence of the central and eastern subcraters (Fig. 12 & 14). Reworked tephra is exposed as volcaniclastic clay beds 20–60 cm–thick within Noisy Nellie and Donald Duck craters and on the lake floor of the 1978 Crater Complex (Fig. 12,

17, & 18).

Within the western subcrater, the level of the hydrothermally active crater lake was seen to fluctuate between field visits in November 2011, June 2012, and June 2013 (Fig. 18). Between the visits in June 2012 & June 2013, a small (20 m diameter) cone formed on the lake floor as a result of small-scale tephra eruption (Table 1). This cone was engulfed by a slight lake level rise prior to the June 2013 visit (Fig. 12 & 18C). The eruptive activity also formed a small lava dome with a spiny surface ("The Gremlin") to the west of the crater lake in late 2012 (Table 1), and was observed actively degassing during the June 2013 visit (as in Fig. 4B).

A scarp on the SW wall of the western subcrater and blocky volcaniclastic mounds within the southern portions of the central and eastern subcraters (Fig. 14) were associated with the 1914 collapse (Fig. 12). The hummocky topography associated with these mounds continues towards the west (e.g. Donald Mound) but is overlain by increasingly thick tephras that were deposited since 1914 (Table 1; Fig. 12). At the head of the 1914 scarp, an arcuate ring fault propagates to the north (Fig. 12). Fumaroles and hot springs occur across the main crater with a high density at the coalescence of the central and eastern subcraters (Fig. 30). Two acid streams drain the central and eastern subcraters and coalesce in the latter before reaching an outlet at Crater Bay (Fig. 1 & 30).

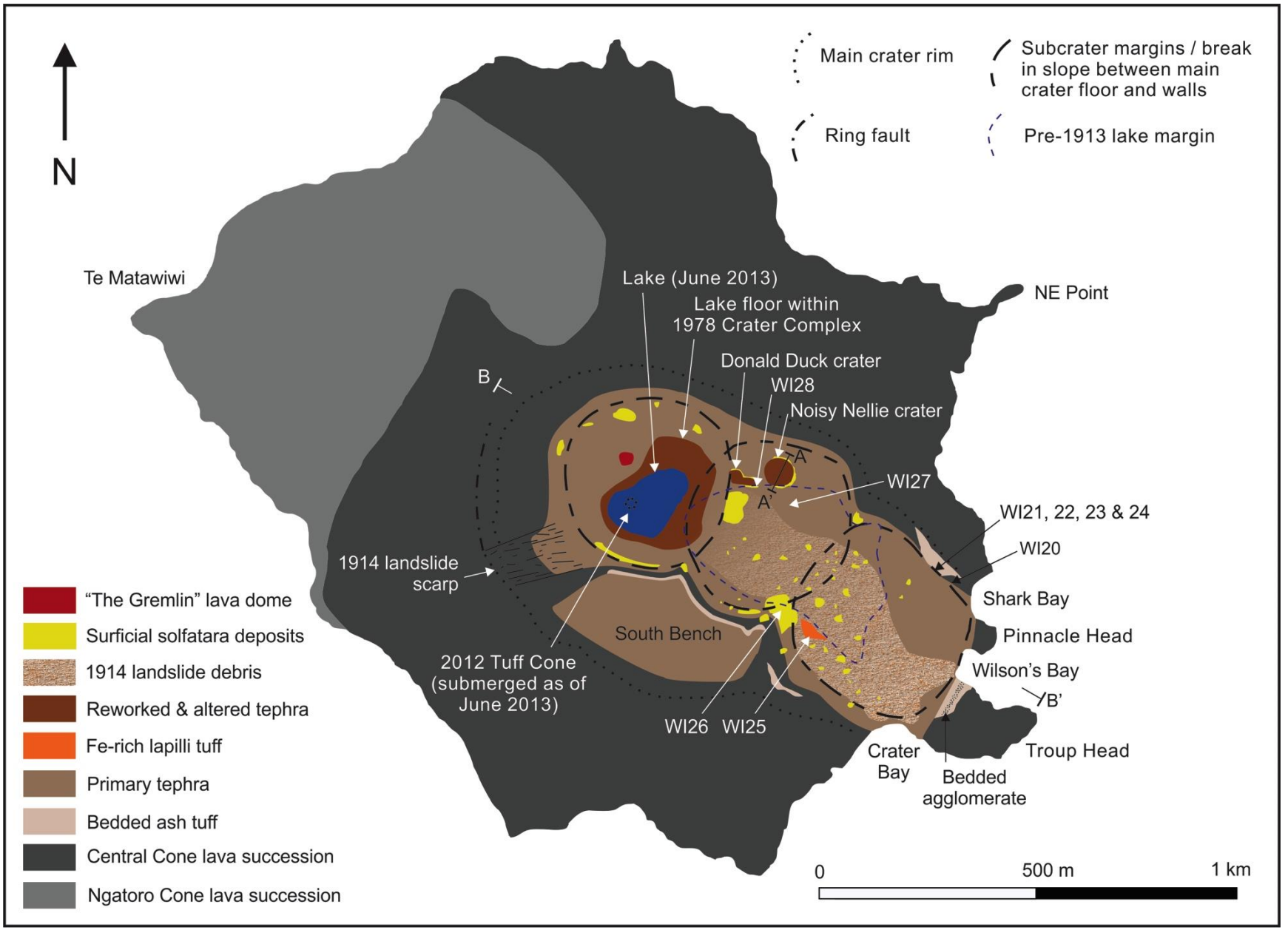

Figure 12 – Geological map of Whakaari showing sample collection sites. Additional lithological units that occur outside the main crater rim, such as historical tephras and volcaniclastics, are excluded for simplicity. Transects A-A' and B-B' correspond to schematic cross-sections presented in Fig. 30 & 32.

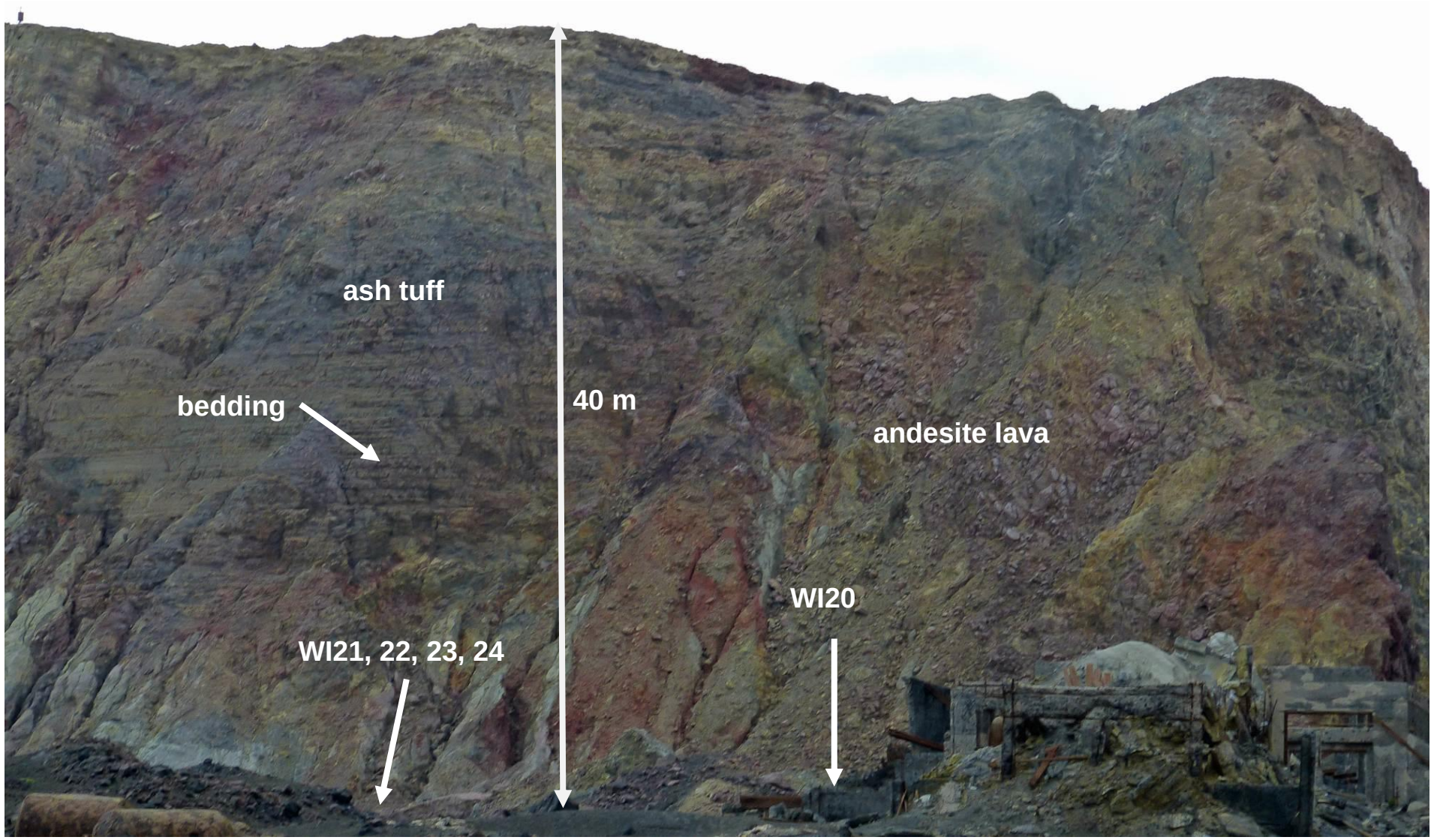

Figure 13 – NE oriented photograph of bedded tuff sequences and lava exposed in Whakaari's NE main crater wall. WI20 (lava), WI21 (fine ash tuff with vertical bubble trains), WI22, WI23 (both fine ash tuff), and WI24 (coarse ash tuff) sample collection sites are labelled (refer to Fig. 12 for map). Note the sulphur factory ruins (right foreground).

Figure 14 – NW oriented photograph of an acid stream bed (foreground) in Whakaari's eastern subcrater. The WI25 (Fe-rich lapilli tuff) sample collection site is labelled (refer to Fig. 12 for map). Note blocky volcaniclastic mounds from the 1914 collapse (mid-right), surficial solfatara deposits on the main crater floor and lower walls (left, right background), and the magmatic gas plume (centre background). Volcanologist for scale.

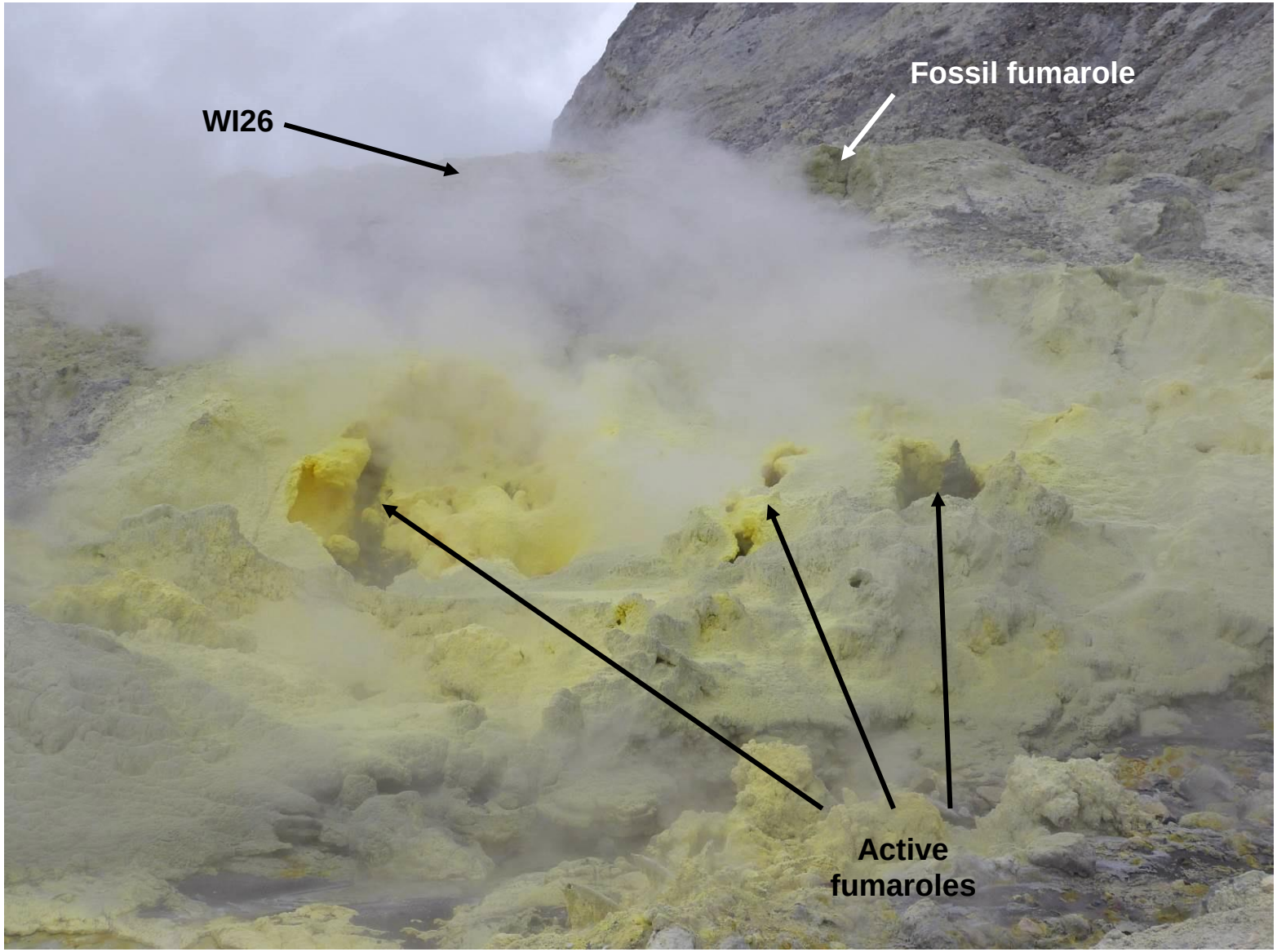

Figure 15 – SW oriented photograph of fumaroles and associated surficial solfatara deposits at the base of the main crater wall where Whakaari's central and eastern subcraters coalesce. Active and fossil fumaroles and the WI26 (surficial solfatara deposit) sample collection site are labelled (refer to Fig. 12 for map).

Figure 16 – NW oriented photograph of primary tephra deposits on Whakaari's main crater floor. White dashed box demarks WI27 sample collection site (refer to Fig. 12 for map).

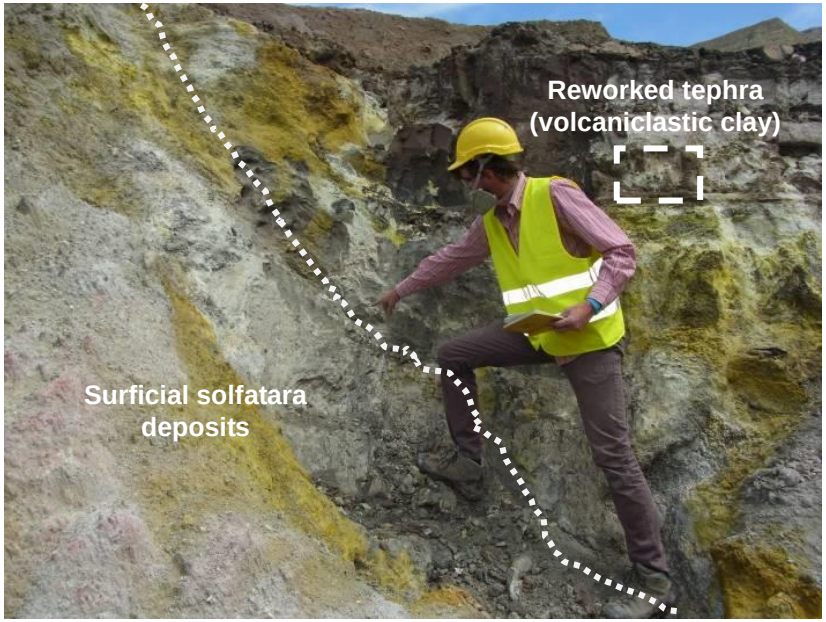

Figure 17 – W oriented photograph of reworked and altered tephra beds (volcaniclastic clay) on-lapping surficial solfatara deposits at the margin of Donald Duck crater. White dashed box demarks WI28 sample collection site (refer to Fig. 12 for map). Author points to true contact between the clay beds and solfatara deposits (white dotted line).

Figure 18 – Photographs of lake level changes within the 1978 Crater Complex. 18A: NW oriented photograph in November 2011. 18B: NW oriented photograph in June 2012. 18C: W oriented photograph in June 2013 (refer Fig. 12 for map). Donald Mound (18A & B, right) is the main crater floor's point of highest elevation (>30 m above sea level) and the exposed lake floor is the lowest (~10 m below sea level).

3.2.2 Sample classification

The connected porosity (and plasticity for the tephras) values referred to in this section are listed in Table 2.

Whakaari cone lava **(WI20):** This sample represented the Central Cone's oldest known lava flow unit (E10, Cole et al, 2000; Table 1) and was inferred to collectively represent Whakaari's cone lavas (i.e. Ngatoro Cone and Central Cone lava successions; Fig. 12). It was collected from a scree slope at the base of an in-situ cliff outcrop on the northern wall of the eastern subcrater (Fig. 12 & 13). It is an intermediate grey, porphyritic, pyroxene-rich andesite, with a low connected porosity (φ = 0.04–0.11) that is controlled by micro- (<1 mm) (φ = 0.04) and macro- (>1 mm) (φ = 0.09–0.11) cracks (Fig. 19A & 19B). Isolated vesicles may exceed 1 mm in size (Fig. 19C).

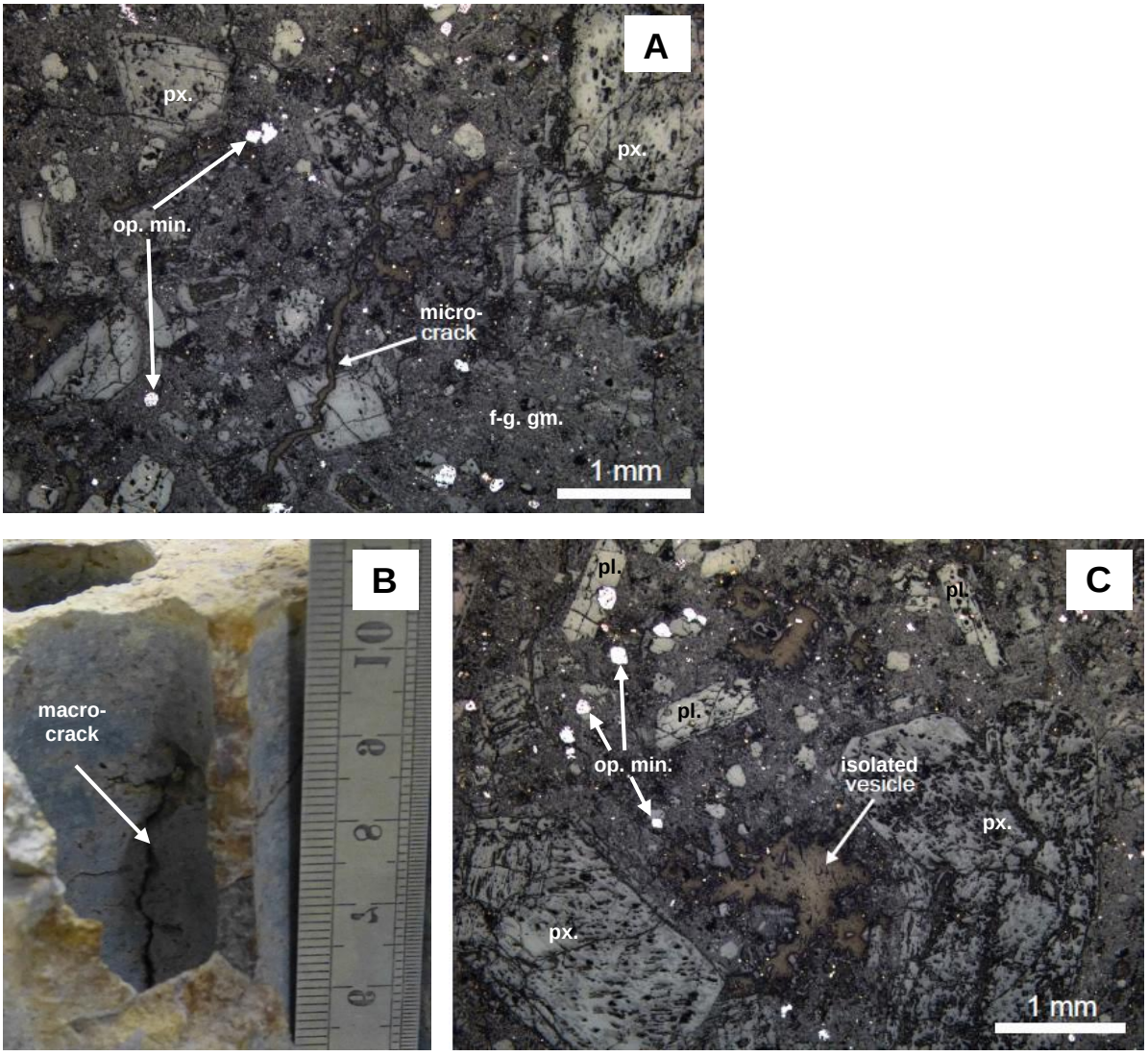

Figure 19 – Photograph and reflected light photomicrographs of Whakaari cone lava (WI20). Micro-cracks (A); macro-cracks (B); and isolated vesicles (C) are labelled. Mineralogy: pl. = plagioclase phenocryst. px. = pyroxene phenocryst. op. min. = opaque minerals. f.g. g.m. = fine-grained groundmass.

***Whakaari fine ash tuff* (WI21, 22, 23):** These samples represented fine ash units within a prehistoric pyroclastic sequence associated with Central Cone. They were collected from a scree slope at the base of an in-situ cliff outcrop on the NE main crater wall (Fig. 12). WI21 is a cream-coloured fine ash tuff, with no visible bedding within the hand sample, and is cemented by amorphous silica, with a moderate connected porosity (φ = 0.32–0.36) associated with 0.2–0.6 mm vertical 'trains' of vesicles visible in hand sample and thin section (Fig. 20A & B). WI22 and WI23 are intermediate-to-light grey fine ash tuffs cemented by amorphous silica, with high connected porosities (φ = 0.42–0.45) controlled by vesicles but no vesicle trains (Fig. 20C, D, E, & F). Alteration of WI23 is apparent in hand sample (Fig. 20E). The presence of alunite, as an additional constituent of the cement in all three samples, was determined by X-ray diffraction (XRD) in a parallel study (Mayer et al, in prep.). Unlike the cone lava (WI20), no micro- or macro-fractures were observed in these, or any other, classified samples. In hand sample, WI22 represented a ~10 cm thick bed (Fig. 20C) and it is clear that when in-situ, WI21 and WI23 are well-bedded (Fig. 13).

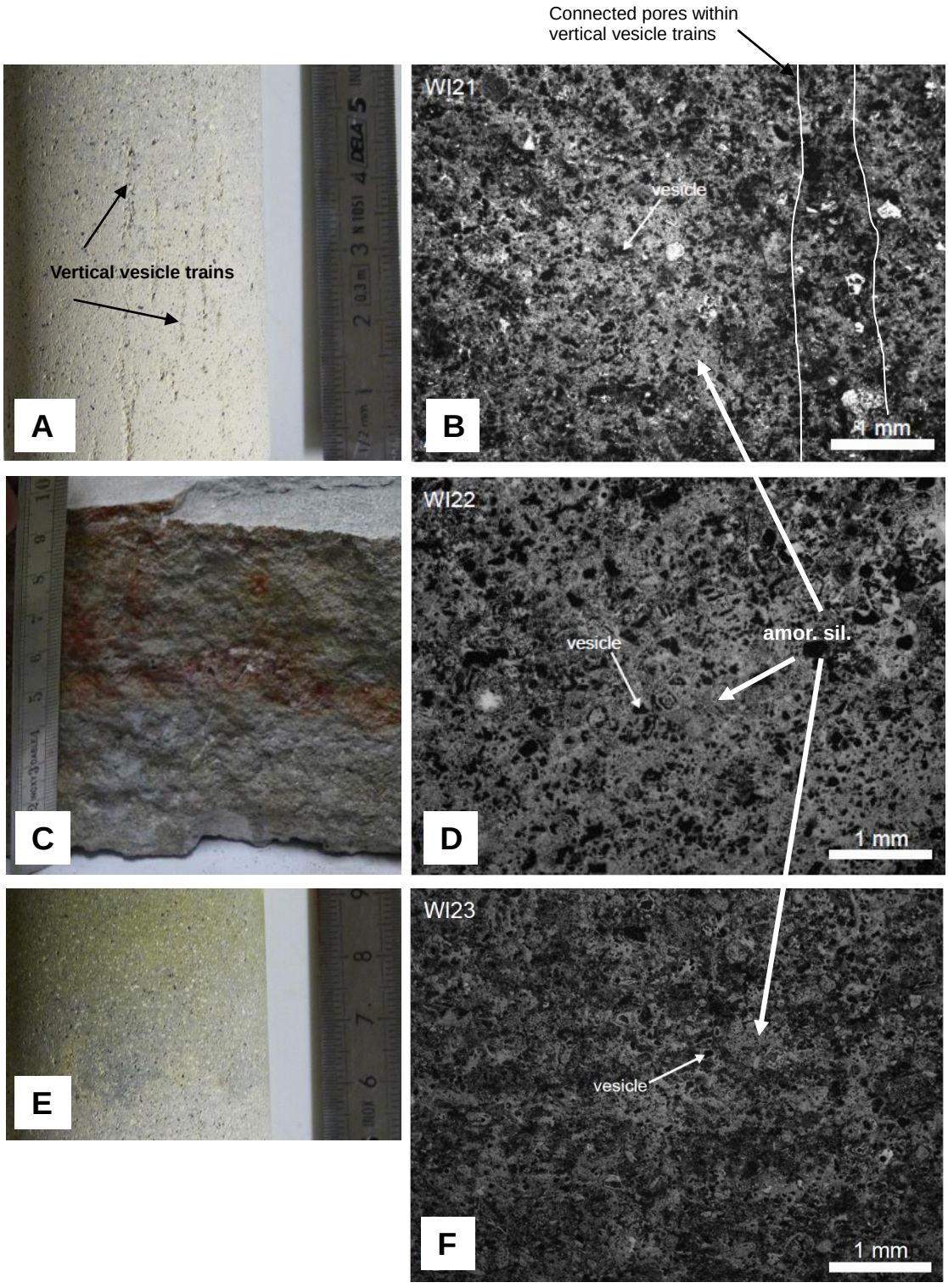

Figure 20 – Photographs and reflected light photomicrographs of Whakaari fine ash tuff (WI21-23). Fine ash tuff with vertical vesicle trains (WI21: A & B). Fine ash tuff (WI22:C & D; WI23: E & F). Mineralogy: amor. sil. = amorphous silica.

***Whakaari coarse ash tuff* (WI24):** This sample represented a coarse ash unit within a prehistoric pyroclastic sequence associated with Central Cone. It was collected from a scree slope at the base of an in-situ cliff outcrop on the NE main crater wall (Fig. 12). It is a light brown coarse ash tuff, with alternating fine ash laminations and a high connected porosity (φ = 0.48) controlled by vesicles (Fig. 21).

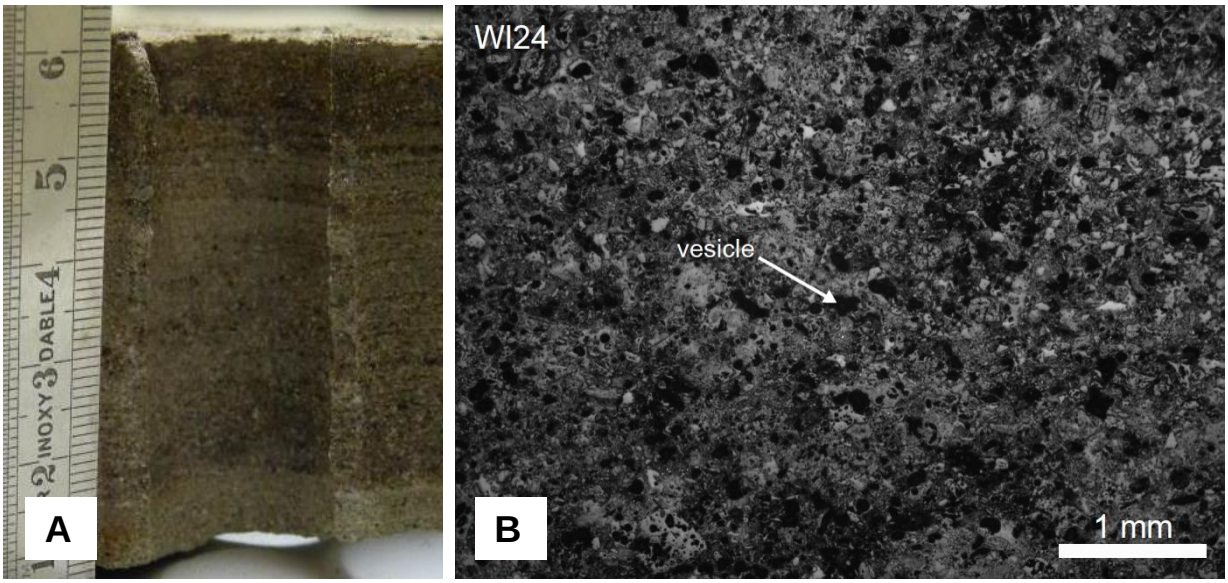

Figure 21 – Photograph (A) and reflected light photomicrograph (B) of Whakaari coarse ash tuff (WI24). Mineralogy: amor. sil. = amorphous silica.

***Whakaari Fe-rich lapilli tuff* (WI25):** This sample represented historic lapilli deposits within an acid stream. It was collected from an acid stream bed on the southern part of the eastern subcrater (Fig. 12). It is a brown lapilli tuff cemented by iron-rich precipitates, with a moderate connected porosity (φ 0.21–0.24) controlled by vesicles (Fig. 22).

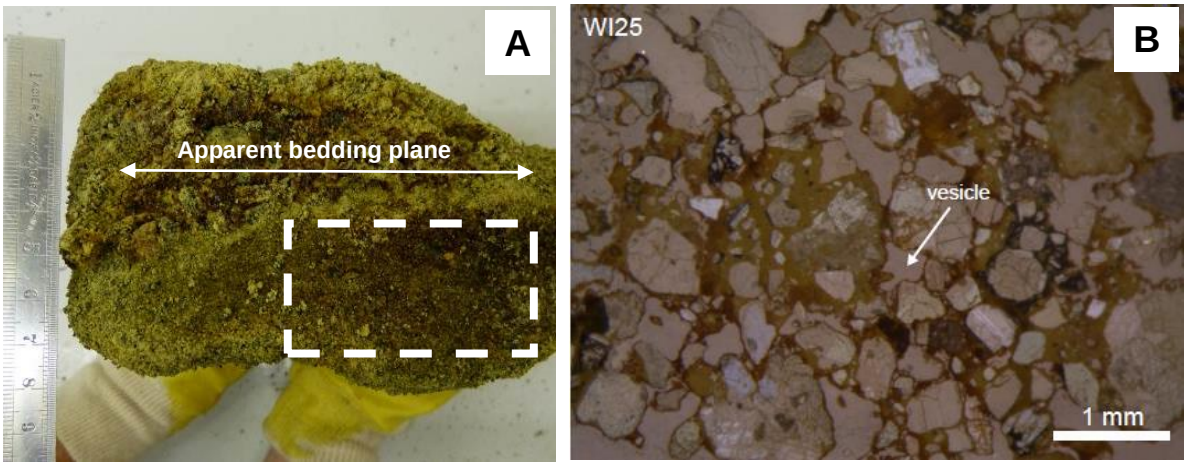

Figure 22 – Photograph (A) and reflected light photomicrograph (B) of Whakaari Fe-rich lapilli tuff (WI25). White dashed box (A) demarks where sample was cored.

***Whakaari surficial solfatara deposit* (WI26):** This sample represented sulphur-rich precipitates atop historical tephra deposits around active and fossil fumaroles. It was collected from the southern section of coalescence of the central and eastern subcraters (Fig. 12 & 16). It is a yellow surficial solfatara deposit, with a moderate connected porosity (φ = 0.21–0.33) controlled by large (>1 mm) vesicles (Fig. 23).

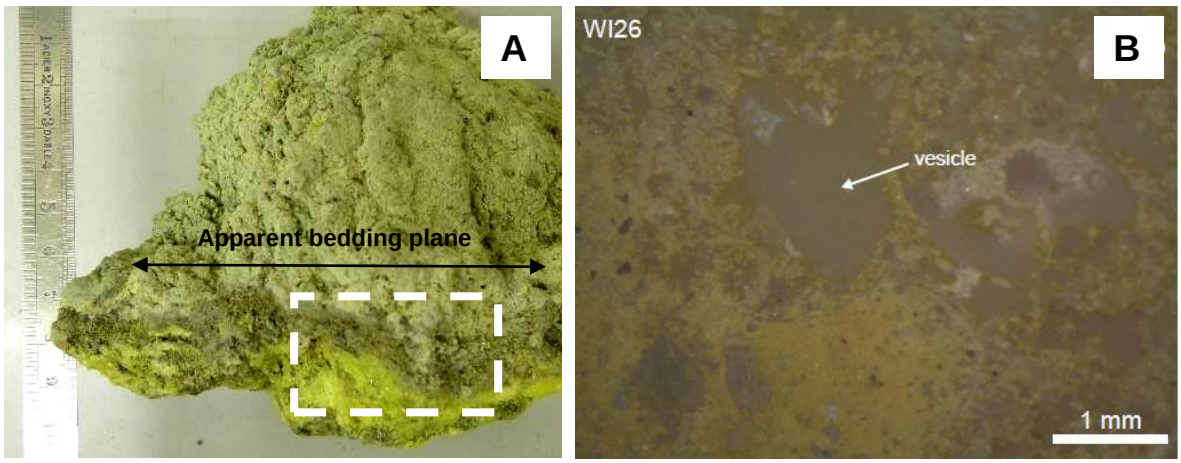

Figure 23 – Photograph (A) and reflected light photomicrograph (B) of Whakaari surficial solfatara deposit (WI26). White dashed box demarks where sample was cored (24A).

***Whakaari primary tephra* ('bulk/main crater fill') (WI27):** This sample represented the most abundant unlithified main crater fill deposit. It was collected at 1 m depth within the central subcrater (Fig. 12 & 16). It is a brown, unconsolidated, non-plastic (PI = 0), poorly sorted, proximal primary tephra comprising 80% coarse ash and 20% lapilli (Fig. 24). The deposit as a whole has a high connected porosity (φ = 0.35) due to its unconsolidated nature.

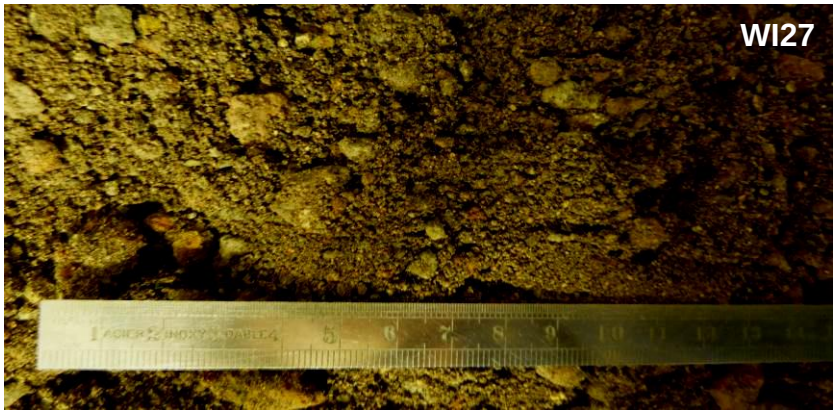

Figure 24 – Photograph of Whakaari primary tephra ('bulk/main crater fill') (WI27).

***Whakaari reworked and altered tephra* (volcaniclastic clay) (WI28):** This sample represented a well-bedded shallow historic eruption crater infill deposit (Fig. 26). It was collected from Donald Duck eruption crater (Fig. 12). It is a brown, very low plasticity slightly plastic (P.I. = 4.2) volcaniclastic clay, with a moderate connected porosity (φ = 0.26) (Fig. 25).

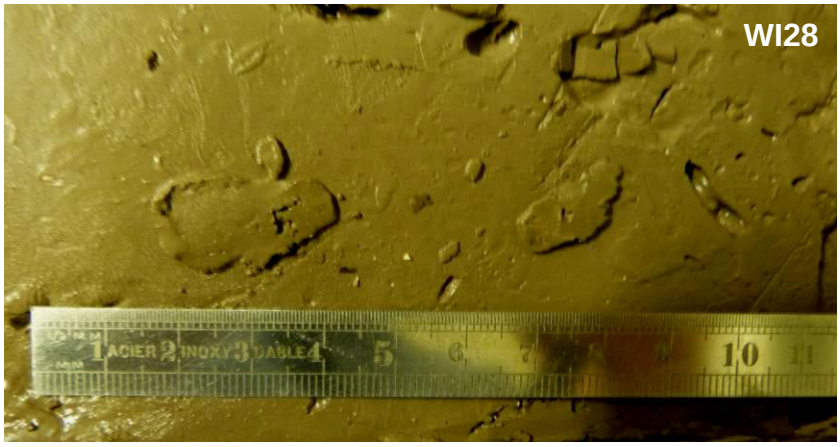

Figure 25 – Photograph of Whakaari reworked volcanic clay after pneumatic consolidation (refer Section 4.1.1).

4.0 Permeability experiments

4.1 Methods

4.1.1 Sample preparation

Samples were cored or molded to 20 x 40 mm cylindrical shapes for permeability experiments. Cylindrical rock samples (WI20-26) were cored to a diameter of 20 mm and precision-ground to a length of 40 mm, dried under vacuum at 40 °C for 24 hours to eliminate any residual pore water, and inserted into a viton jacket. Rock core descriptions, including their orientations where approprirate, are listed in Table 2. Cone lavas were cored parallel to micro- and macro-cracks (Fig. 19), fine ash tuffs with vertical vesicle trains were cored with the vesicles in the vertical (in-situ) and horizontal orientations (Fig. 20), and Fe-rich lapilli tuff and solfatara deposits were cored perpendicular and parallel to their apparent in-situ bedding planes (Fig. 22 & 23). Primary tephra was sieved to remove any lapilli that were >20 mm, dried under vacuum at 40 °C for 24 hours, and poured into a 20 mm diameter cylindrical shaped viton jacket to 40 mm depth, with no tamping, in order to approximate field consolidation. Reworked tephra/volcaniclastic clay was pneumatically consolidated at 200 kPa for 48 hours, rather than vacuum dried, to minimise the water content but avoid the growth of shrinkage cracks, as these would erroneously increase the permeability. The pneumatic consolidation unavoidably decreased the connected porosity of the volcanic clay. Assuming a soil unit weight of 20 kN/m^3, this consolidation was equivalent to a depth of ~20 m (Holtz et al, 2011) and therefore is directly relevant to shallow subsurface clays at Whakaari. The sample was then cored with a cylindrical cutter of 40 mm length and 20 mm diameter, and placed inside a viton jacket.

4.1.2 Units

For the calculations associated with Equations 1–5, the International System of Units (SI) was utilised where appropriate (IBWM, 2006).

4.1.3 Argon gas permeability (k_{Ar}) and Darcy's law

Argon gas permeability (k_{Ar}) experiments were performed on the prepared samples at room temperature (25 °C) in a high-pressure vessel at the University of Strasbourg (Fig. 26). The viton jacket was clamped onto end-pieces in the experimental set-up and a modified form of Darcy's law (Darcy, 1856) was applied to take compressibility of argon gas into account. Thus, k_{Ar} was derived from the following expression (Scheidegger, 1974):

$$\frac{Q}{A} = \frac{k_{Ar}}{vL} \frac{P_{up}^2 - P_{down}^2}{2P_{down}} \qquad (1)$$

where Q is the volume of fluid measured per unit time, A is the cross-sectional area of the sample, v is the gas viscosity (v = 2.21 x 10^{-5} Pa.s for Ar), L is the length of the sample, and P_{up} and P_{down} are the pore fluid pressures at the upper and lower ends of the sample, respectively. To ensure no gas flow occurred between the viton jacket and the sample, a constant confining pressure was applied at 0.5 MPa for soil samples (WI27 & 28), 1 MPa for 'weak' rock samples (WI25 & 26), and 2 MPa for 'strong' rock samples (WI20-24). Samples WI20-27 were initially subjected to steady-state gas flow (Table 2) in which the differential pore pressure P_{up} - P_{down} between the upstream and the downstream sides of the sample was kept constant (with the downstream flow rate monitored by a gas flow meter). Due to the very low expected permeability value of clay, WI28 was subject to transient gas flow in

which the initial differential pore pressure re-equilibrated by fluid flow once the upstream fluid pressure inlet was closed (in this case, the differential pore pressure decay was monitored). For all experiments, P_{up} - P_{down} never exceeded 0.4 MPa (P_{down} was the ambient atmospheric pressure [0.1 MPa]; P_{up} did not exceed 0.5 MPa).

4.1.4 Forcheimer and Klinkenberg corrections

Experiments on samples to which the Forcheimer or Klinkenberg corrections were applied are listed in Table 2.

Darcy's law (Equation 1) is only valid when fluid flow is laminar. When Q is high, inertial effects cause disproportionality between Q and the driving pressure $(P_{up}^2 - P_{down}^2)/P_{down}$. As a result, the apparent k_{Ar} deduced from Equation 1 varies with Q. To correct for deviations from Darcy's law at high gas flow rates, the empirical Forchheimer (1901) relationship was combined with Equation 1 (Wu & Firoozabadi, 2011):

$$\frac{1}{k_F} = \frac{1}{k_{Ar}} - \beta Q \qquad (2)$$

where k_{Ar} is the apparent gas permeability (Equation 1), k_F is the corrected gas permeability, and β is a parameter dependent on η, P_{down}, and the sample geometry.

Darcy's law (Equation 1) may not apply for gas flow at low pressures. For example, in thin cracks where the mean free path of a gas molecule becomes comparable to the mean distance between crack walls, the no-slip boundary condition on the crack surface inherent to Darcy's law is no longer valid. Gas molecules move along the crack surface and enhance Q. To

account for the additional flux due to the gas flow at the wall surface, the Klinkenberg (1941) correction allowed the determination of k_{Ar}:

$$k_{Ar} = k_{app}\left(1 + \frac{2b}{P_{up} + P_{down}}\right) \qquad (3)$$

where k_{Ar} is the argon gas permeability, b is Klinkenberg's slip factor, and k_{app} is k_{Ar} from Equation 1.

4.1.5 Intrinsic gas permeability (k_{gas}) and approximate hydraulic conductivity (K_{water})

To calculate the intrinsic gas permeability k_{gas} from measurements without running multiple tests at various pore fluid pressures, single measurements were made by the transient method as suggested by Brace et al (1968). An initial increase (0.5 MPa) of P_{up} was applied to the sample and the fluid inlet closed. By using the mass balance equation and introducing an average pore pressure gradient inside the sample, the intrinsic gas permeability k_{gas} was calculated from the upstream pore pressure decay as follows:

$$k_{gas} = 2\frac{\eta L}{A}\frac{V_{up}}{P_{up^2} - P_{down^2}}\frac{dP_{up}}{dt} \qquad (4)$$

where V_{up} is the volume of the upstream fluid pressure circuit (in this case, 7.0 x 10^{-6} m^3). Since P_{down} is constant (ambient), the temporal decay of P_{up} corresponds to a decay of the mean pore pressure (P_{up} + P_{down})/2. Thus the dependence of k_{gas} with (P_{up} + P_{down}) was obtained to check the Klinkenberg effect by applying Equation 3, and used to derive the intrinsic gas permeability k_{gas}. The principle of k_{gas} is that it should be an intrinsic property of

the rock or soil that is independent of the density and viscosity of the fluid. Assuming there was no interaction between fluid and rock during the experiments, k_{gas} was used to approximate the hydraulic conductivity K_{water} as follows (Bear, 1988):

$$Kwater = k.\rho\frac{g}{\nu} \qquad (5)$$

where ρ is the density of water (997.05 kg/m^3 at 25 °C), g is the standard acceleration of gravity (9.81 m/s^2), and ν is the viscosity of water (8.91 x 10^{-4} kg/ms^{-1} at 25 °C).

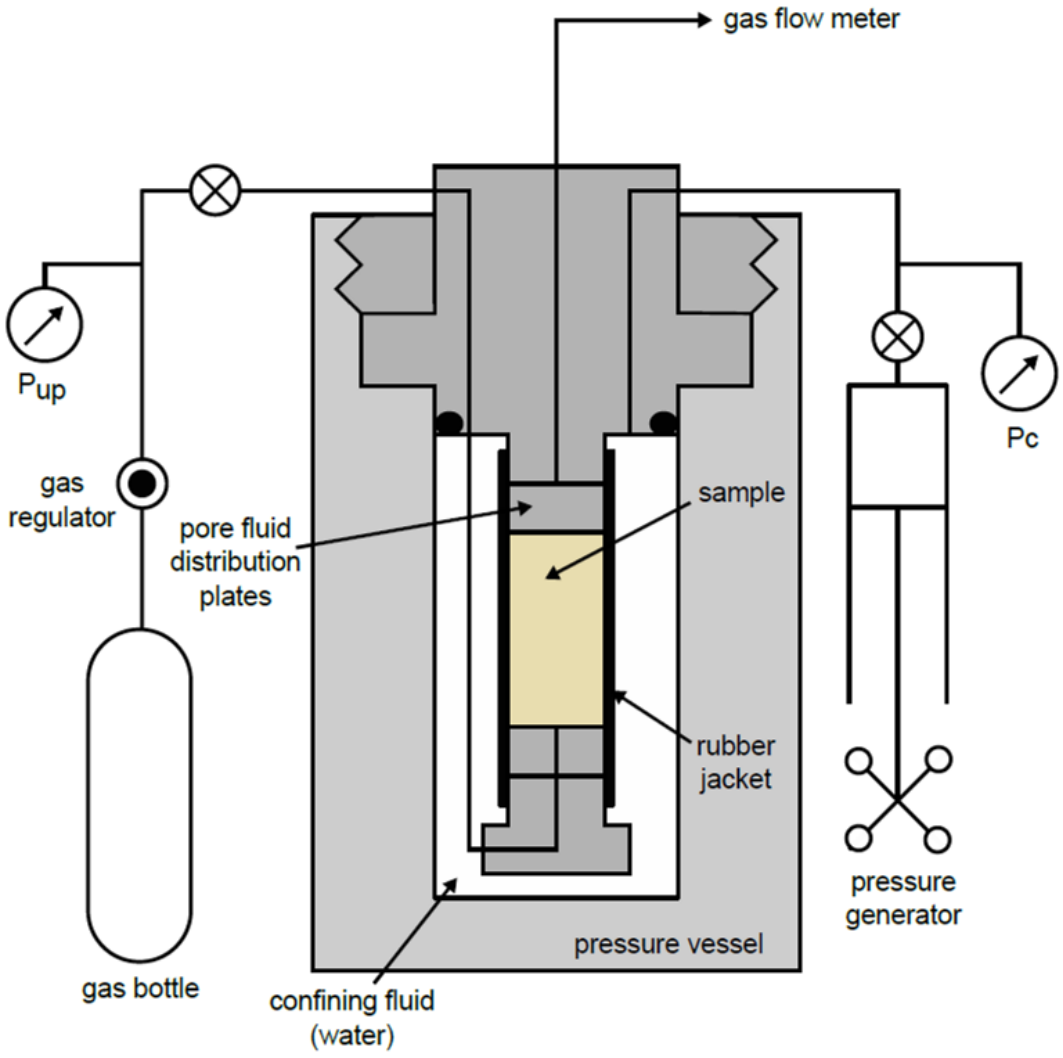

Figure 26 – Diagram of the experimental set-up for determining the intrinsic gas permeability.

4.2 Results

The experimental results are summarised in Table 2. Comparisons of the hydraulic conductivity and gas permeability results (against connected porosity) (Fig. 27 & 28) indicate that the permeability relationships of Whakaari's main crater lithologies remain the same, regardless of whether the fluid flow is gas or liquid water phase. Cracks control the permeability of cone lavas. Macro-cracked cone lavas (k_{gas} = 1.38E-014–1.04E-013 m^2) were approximately one-to-two orders of magnitude more permeable than micro-cracked cone lavas (k_{gas} = 1.58E-016 m^2). Grain-size and vertical trains of vesicles control the permeability of ash tuffs. Fine ash tuffs had a low-to-moderate permeability (k_{gas} = 7.27E-016–3.14E-015 m^2) and coarse ash tuff had high permeability (k_{gas} = 3.08E-013 m^2). The fine ash tuffs with vertical trains of vesicles were anisotropic with a slightly higher permeability (k_{gas} = 3.09E-015 m^2) than when vesicle trains were horizontal/perpendicular to fluid flow (k_{gas} = 7.27E-016 m^2). Fe-rich lapilli tuffs were anisotropic with a slightly higher permeability along the orientation parallel to apparent bedding (k_{gas} = 3.04E-12 m^2) than perpendicular to it (k_{gas} = 2.63E-12 m^2). Surficial solfatara deposits were also anisotropic, with a slightly higher permeability along the orientation parallel to apparent bedding (k_{gas} = 1.75E-12 m^2) than perpendicular to it (k_{gas} = 3.99E-13–1.11E-12 m^2). The primary tephra/unlithified main crater fill had the highest permeability (k_{gas} = 3.36E-12 m^2) of all Whakaari's main crater lithologies. Reworked tephra/volcaniclastic clay was ~7 orders of magnitude less permeable than main crater fill (k_{gas} = 4.50E-19 m^2).

Table 2 – Results of plasticity, connected porosity, and gas permeability experiments on samples representing Whakaari's main crater lithologies. 'bedding' = apparent bedding. Mois. cont. = moisture content. **ϕ** = connected porosity. Conf. press. = confining pressure applied during permeability experiments. 'Klink.' and 'Forch.' = Klinkenberg and Forcheimer corrections, respectively. k_{gas} = gas permeability. K_{water} = hydraulic conductivity.

Sample	Core description	Moist. cont. (%)	Plasticity index	ϕ	Conf. press. (MPa)	Correction	k_{gas} (m^2)	K_{water} (ms^{-1})
WI20-1	Micro-cracked cone lava	-	-	0.04	2	Klink.	1.58E-16	1.73E-9
WI20-Z-D	Macro-cracked cone lava	-	-	0.09	2	Forch.	1.38E-14	1.51E-7
WI20-Z-E	Macro-cracked cone lava	-	-	0.11	2	Forch.	1.04E-13	1.14E-6
WI21-Y-A	Fine ash tuff with horizontal trains of vesicles	-	-	0.36	2	Klink.	7.27E-16	7.98E-9
WI21-Z-A	Fine ash tuff with vertical trains of vesicles	-	-	0.32	2	Klink.	3.09E-15	3.39E-8
WI22-Z-A	Fine ash tuff	-	-	0.45	2	Klink.	3.14E-15	3.45E-8
WI23-Z-A	Fine ash tuff	-	-	0.42	2	Klink.	1.21E-15	1.33E-8
WI24-Z-A	Coarse ash tuff	-	-	0.48	2	Forch.	3.08E-13	3.38E-6
WI25-Y-A	Fe-rich lapilli tuff parallel to 'bedding'	-	-	0.21	1	Forch.	3.04E-12	3.34E-5
WI25-Z-A	Fe-rich lapilli tuff perpendicular to 'bedding'	-	-	0.24	1	Forch.	2.63E-12	2.89E-5
WI26-Y-A	S-rich solfatara deposit parallel to 'bedding'	-	-	0.33	1	Forch.	1.75E-12	1.92E-5
WI26-Z-A	S-rich solfatara deposit perpendicular to 'bedding'	-	-	0.3	1	Forch.	1.11E-12	1.22E-5
WI26-Z-A	S-rich solfatara deposit perpendicular to 'bedding'	-	-	0.21	1	Forch.	3.99E-13	4.38E-6
WI27	Primary tephra (main crater fill)	7	0	0.35	0.5	Forch.	3.36E-12	3.69E-5
WI28	Reworked & altered tephra (volcaniclastic clay)	42	4.2	0.26	0.5	-	4.50E-19	4.94E-12

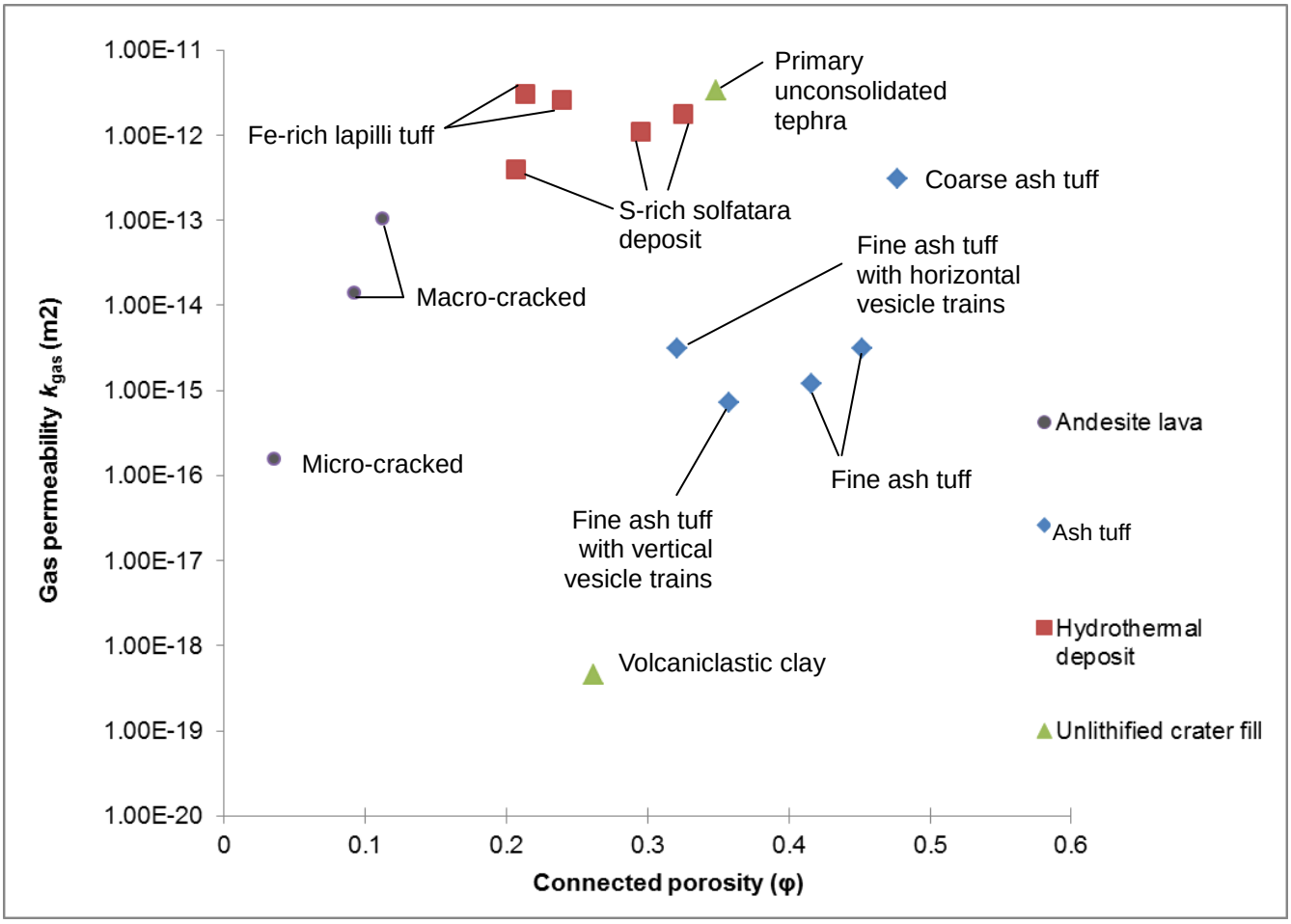

Figure 27 – Graph of gas permeability and connected porosity of Whakaari main crater samples.

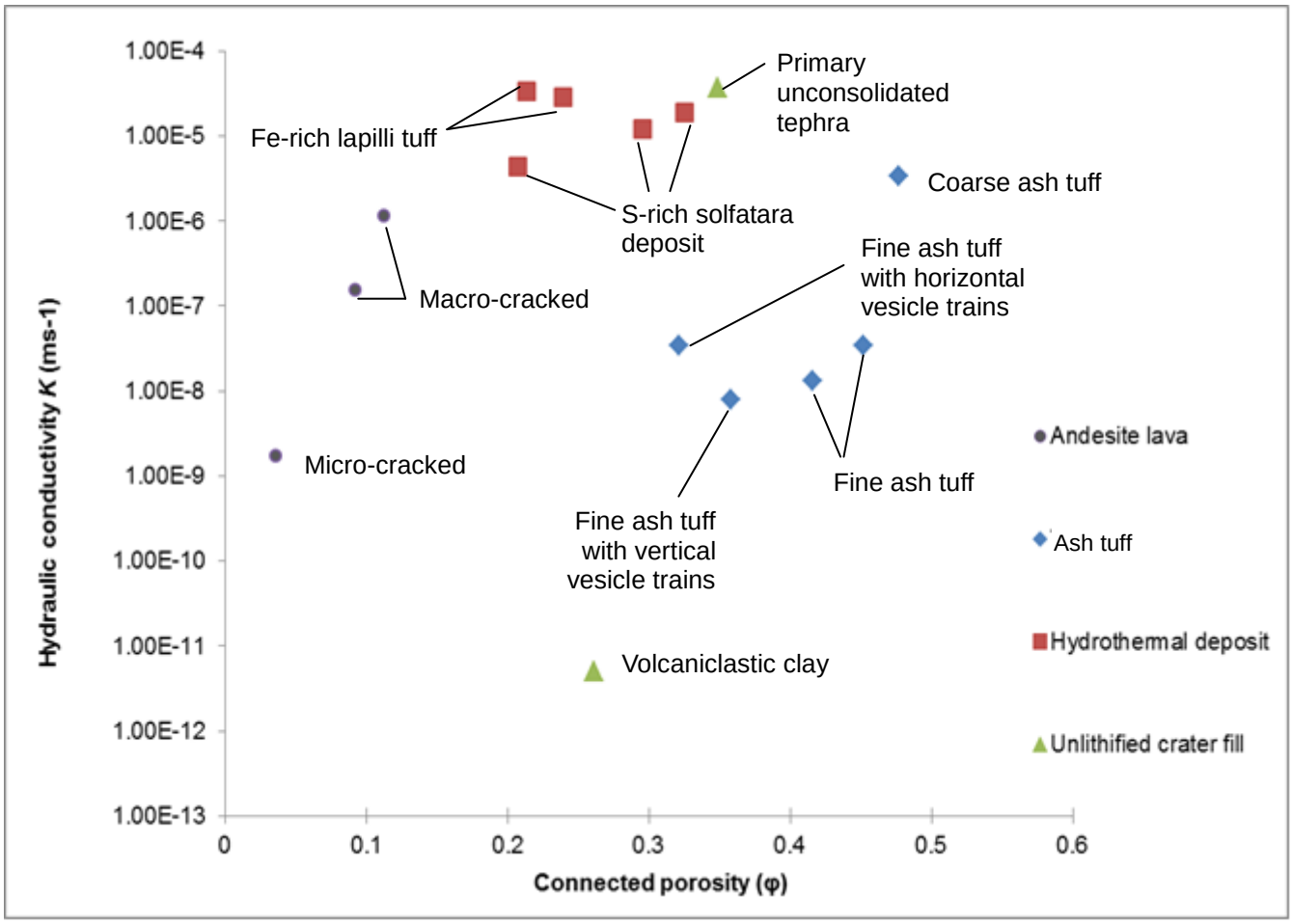

Figure 28 – Graph of hydraulic conductivity and connected porosity of Whakaari main crater samples.

5.0 Summary of field and experimental results

This study's results have shown that:

(a) Whakaari's main crater geology can be subdivided into prehistoric (pre-1826) tuffs and cone lavas exposed in the crater walls, and historic tephras, Fe-rich lapilli tuffs, and surficial solfatara deposits on the crater floor (Fig. 12);

(b) The distributions of historic tephras that have been reworked/altered are controlled by processes associated with historic eruption cratering and re-deposition within crater lakes (Fig. 12; after Fig. 9, 10, & 11A).

(c) The connected porosity of cone lavas is controlled by cracks, and connected porosity of tuffs and surficial solfatara deposits is controlled by vesicle distribution due to cementation (Section 3.2.2);

(d) The permeability of the Whakaari lithologies varies across ~7 orders of magnitude: primary tephras/unlithified main crater fill > (= 'more permeable than') Fe-rich lapilli tuffs > surficial solfatara deposits > coarse ash tuffs > macro-cracked cone lavas > fine ash tuffs > micro-cracked cone lavas > reworked tephras/volcaniclastic clay (Table 2; Fig. 27 & 28).

6.0 Discussion

6.1 Significance of the prehistoric (≤3.4 ka) sector collapse

The prehistoric sector collapse was significant for fluid flow at Whakaari and may have influenced the occurrence of wet versus dry eruptions. The youngest lava flow is truncated by the main crater (Moon et al, 2009) and radiometric dating shows this lava was erupted between 3.4–2.6 ka (Table 1). Therefore, large scale structural and morphological modification during and subsequent to the $2.1x10^8$ m^3 prehistoric sector collapse must have occurred ≤3.4 ka (Table 1). Removal of low permeability cone lava (Table 2) was likely to have significantly increased seawater infiltration into the high permeability, unlithified, main crater fill above the magma conduit (Fig. 32). In addition, the newly-opened amphitheatre-like morphology of the main crater became a catchment basin for rainfall, thus favouring the collection of meteoric water in lakes – also above the magma conduit (Fig. 9, 11A, & 18). Therefore, it is proposed in this study that a ≤3.4 ka sector collapse (Moon et al., 2009) instigated a major change to Whakaari's fluid flow system, allowing influx of water above the magma conduit and leading to its present susceptibility to wet eruptions. A semi-schematic 3-dimensional model to explain this is presented in Figure 29. Similar large structural changes in edifice morphology may be important for controlling wet phreatic/phreatomagmatic versus dry magmatic behaviour at other volcanoes worldwide.

While the present hydrological regime at Whakaari favours phreatic or phreatomagmatic eruptions, magmatic eruptions may also occur (Fig. 4A & B). If an intrusion of magma incrementally heats and dries the saturated main crater fill, then the conditions for phreatic or phreatomagmatic fragmentation may be avoided. Such a process was likely a dominant factor

during the extrusion of the 2012 lava dome ("The Gremlin") (Fig. 4B), as the nearby lake was observed drying up prior to the eruption (GeoNet, 2012; Chardot et al., in prep). However, there has been a lack of lava flows at Whakaari within the last 3.4 ka, whereas prior the estimated return period for a lava flow eruption was 0.5-1.5 ka (Cole et al, 2000). It is possible that the sector-collapse related influx of water above the magma conduit may have also hindered the eruption of lava flows.

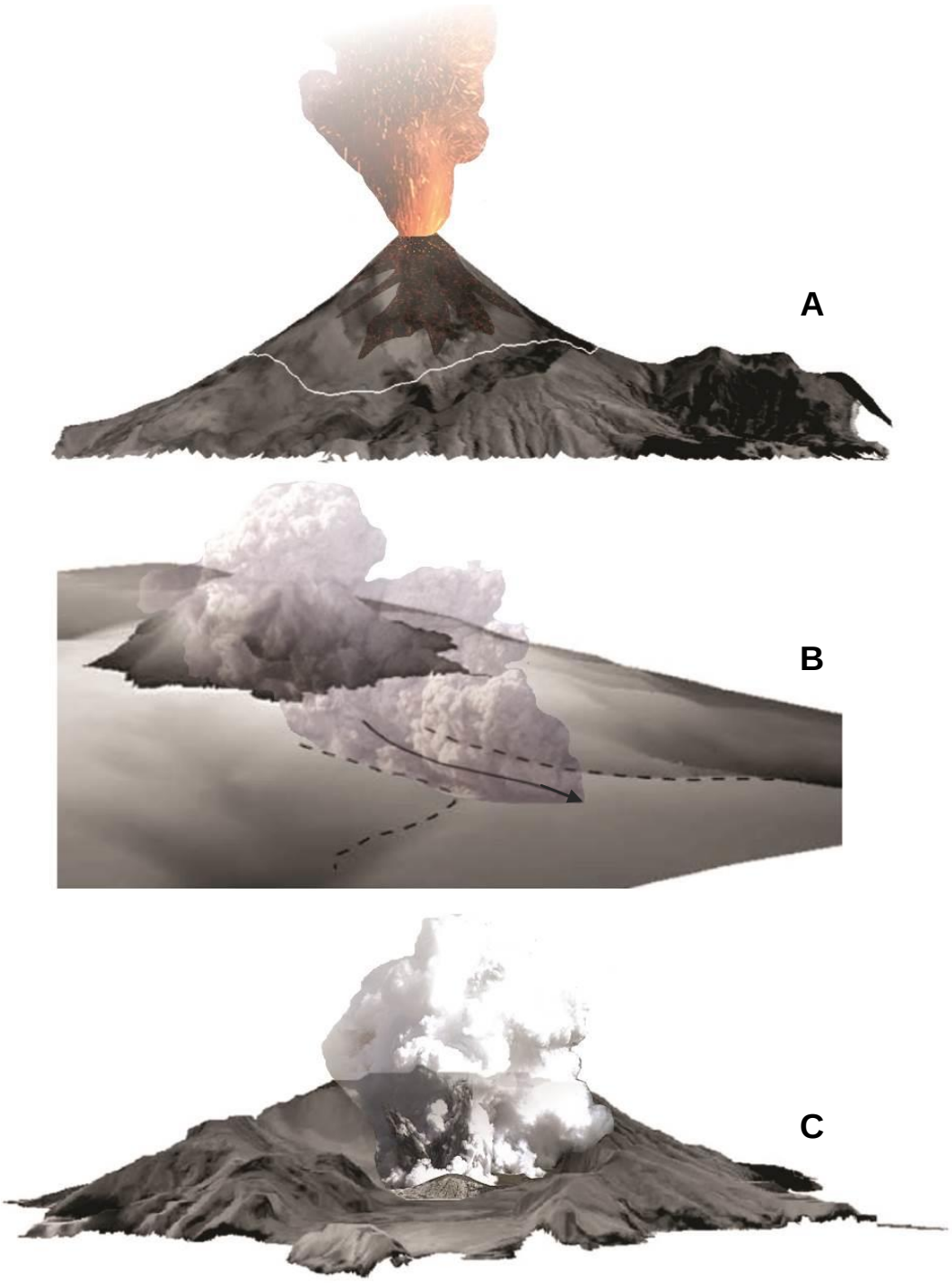

Figure 29 – Semi-schematic 3D model of the formation of Whakaari's modern main crater and fluid flow system. Magmatic eruptions produced lava flows that built Central Cone to ~650 m (A), before a summit of hydrothermally weakened lava collapsed (B) (white line demarks boundary of weakened rock). The subsequent debris avalanche created modern bathymetry to the east of the island (B), leaving the modern crater's flat-floored amphitheatre-like morphology (C). This allowed seawater infiltration and favoured meteoric water collection, possibly causing a susceptibility towards phreatic and phreatomagmatic eruptions (C). Modified from Moon et al (2009).

6.2 Fluid flow within the modern main crater

Variations in Whakaari's vertical and lateral fluid flow, through both diffuse and concentrated pathways, are constrained by the lithology and structure of the modern main crater. Based on (a) the spatial distribution of surface geological units exposed on the floor and walls of the main crater (Fig. 12), (b) fluid flow pathways associated with subcraters and eruption craters (Fig. 30 & 31), and (c) experimental data, a schematic model of fluid flow within Whakaari's main crater is proposed in Figure 32.

Vertical degassing and re-circulation throughout Whakaari's main crater, and lateral seawater infiltration from the east, is accommodated through high permeability main crater fill (Fig. 32). Cone lavas formed by prehistoric eruptions focus vertical fluid flow through the main crater (Fig. 1). However, discontinuities cross-cut the main crater stratigraphy at subcrater and eruption crater margins, preventing laterally continuous beds and facilitating vertical fluid flow (Fig. 32). Despite frequent crater formation (Fig. 31), the surface of the main crater floor remains relatively flat due to erosion and re-deposition of loose tephra deposits (Fig. 32). Local clay 'seals' of very low permeability (Fig. 10), apparently formed by lacustrine sedimentation together with eruption crater infilling and sorting processes, divert diffuse gas flow to remnant eruption crater margins (Fig. 31).

The prehistoric subcraters are an observed structural constraint on fluid flow. The mass and heat flux anomalies, discovered by Mongillo and Wood (1995) and Bloomberg (2012), illustrate a permeability control at the subcrater margins. However, since all exposed deposits on the floors of the subcraters are from historical eruptions, there are no observable lithological or structural fluid flow constraints at the surface (Fig. 1 & 12). Surficial solfatara

deposits, which are localised at subcrater margins (Fig. 12), occur due to the precipitation of sulphur-rich minerals from fumarolic discharge and hence are a *consequence* of the higher fluid flow in these regions. It is inferred in this study that structural and morphological modification continued after the large <3.4 ka collapse with a series of smaller cratering events and landslides forming and modifying the subcraters. The alignment of the subcraters in a NW-SE orientation suggests that 12.6 ± 3.5 mm yr^{-1} regional NW-SE extension (Lamarche et al, 2006) may have also contributed to this structural and morphological evolution. The ≤3.4 ka sector collapse likely lowered the crater floor to a level similar to that observed today (Moon et al, 2009). Decompression of the magma conduit due to mass removal, and subsequent influx of seawater, may have directly caused explosive eruptions that excavated the western, central, and eastern subcraters. Two prehistoric craters that may be associated with eruptions have been previously inferred within the eastern subcrater by Mongillo & Wood (1995), but this study found no field volcanological evidence for structural or lithological similarities to historic eruption craters. It is likely that if these are in fact prehistoric eruption craters, they have been buried by eruption deposits and volcaniclastics since formation (Fig. 32).

There is a correlation between (a) the foci of concentrated vertical gas and water flow through fumaroles and hot springs (mapped in this study); (b) the epicentres of shallow (<1 km depth) earthquakes recorded during the Nishi et al (1996) study; (c) diffuse degassing through unlithified main crater fill (Bloomberg, 2012); and (d) the coalescence of the central and eastern subcraters as defined by thermal anomalies (Mongillo & Wood, 1995). The coalescence of the central and eastern subcraters is therefore inferred to be an important boundary for fluid flow, where [perhaps violent] rapid heating and subsequent rise of laterally infiltrating seawater may prevent it moving further westward through the main crater in large

volumes (Fig. 32). This hypothesis provides an explanation for why Giggenbach et al (2003) and Bloomberg (2012) found that the isotopic seawater contribution in acid hot springs is significantly higher towards the east.

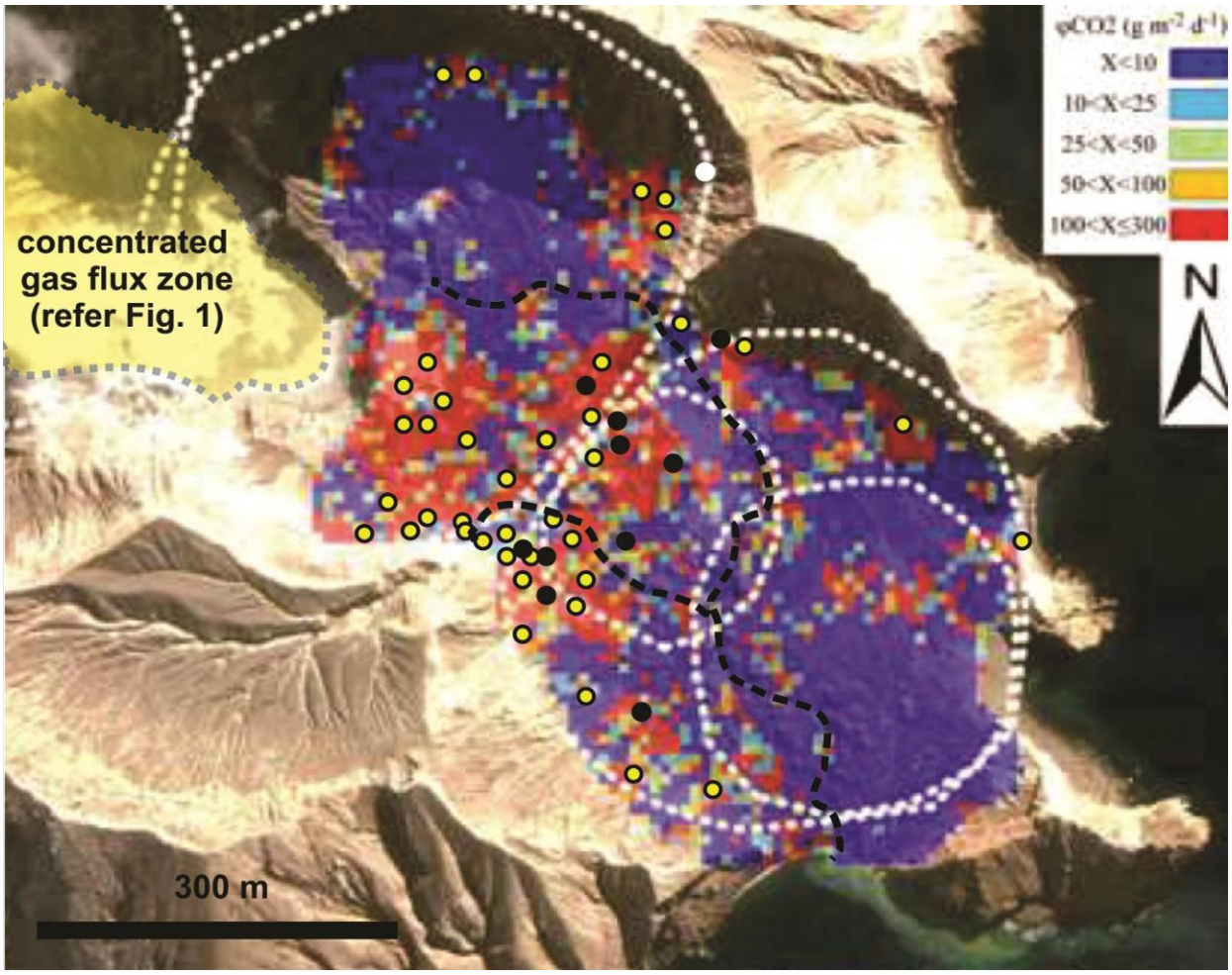

Figure 30 – Structural map of fluid flow in Whakaari's central and eastern subcraters. Fumaroles (yellow filled circles), hot springs (black filled circles), and acid streams (black dashed lines) are mapped with prehistoric craters (white dotted lines) (Mongillo & Wood, 1995) and φCO_2 flux isopleths (Bloomberg, 2012). Note the high fluid flow at coalescence of the central and eastern subcraters. Modified after Bloomberg (2012).

The high vertical fluid flow observed at the margins of subcraters (Fig. 30) and eruption craters (Fig. 10) may be explained by the relative ages of crater infill deposits. Specifically, these relative ages result in a juxtaposition of lithologies with differences in compaction, alteration, and mineralisation within pores, which influences permeability (Table 2). The eruption cratering process disrupts and excavates tephra to produce a temporary permeable pathway that focuses subsequent vertical fluid flow. Over several months to years, the permeability of such a pathway will decrease due to eruption crater infilling, consolidation of the infill material, and mineralisation of pore space. A model for this is presented in Figure 31, based on the uppermost geology of the 1978 Crater Complex, Donald Duck, and Noisy Nellie craters (Fig. 12), previous volcanological models (Houghton & Nairn, 1989), previous observations (Fig. 7–10), and the results of analogue experiments (Roche et al, 2001). This model is then adapted for overlapping eruption crater structures (Fig. 6) within the greater main crater model (Fig. 32). The age-related effects of consolidation and mineralisation reducing permeability are schematically represented by buried eruption craters in the central and eastern subcraters (Fig. 32). Geochemical analysis of ejecta at Whakaari has shown that "alteration produces a characteristic suite of minerals dominated by silica and sulfates," including anhydrite, alunite, and pyrite (Wood, 1994). Fluid flow is increasingly focussed at crater wall discontinuities (Fig. 32). Subsequent eruptions and subsidence from the same vent result in further disruption and excavation and continued concentration of vertical fluid flow pathways (Fig. 6). Hence, vertical fluid flow remains focussed at the western subcrater through historical time (Fig. 32).

The tuffs (WI21-24) provide insight into the likely lithologies currently at depth at Whakaari. Similar layers with low-medium permeability (Table 2) probably exert significant control on the vertical movement of fluids at depth (Fig. 32). The tuff sequences exposed high in main

crater walls today (Fig. 13) may represent deep main crater fill that was altered and lithified prior to the ≤3.4 ka sector collapse(s), when Central Cone's edifice stood at a higher elevation – Moon et al (2009) estimated ~650 m above sea level. Hence, these tuff sequences were at that time located several hundred metres below the surface of the pre-collapse main crater but are now exposed post-collapse. Fine ash tuffs are likely to be the most important lithological control on the main crater's subsurface fluid flow, due to their low-to-medium permeability. 'Paralava' bombs (Wood & Browne, 1996) consisting of halite-cemented crater-lake sediments that were ejected on January 25 1987 provide further convincing evidence that similarly altered tuffs make up much of the subsurface structure of Whakaari's main crater. Wood & Browne (1996) found that the bombs were likely to have originated at 830-1000°C under a pressure of <5 MPa; therefore altered tuffs may be inferred to be present to <500 m depth.

Within the lowest elevation of the western subcrater, clay is saturated by lake water to above its liquid limit (Fig. 32). Focussed vertical gas flow overcomes the cohesive strength of this saturated clay, thereby allowing thermal fluids to rise through the lake water despite clay's very low permeability (Table 2). This prevents fluid flow from localising at the crater margins and continuously feeds Whakaari's gas and steam plume (Fig. 1). A similar process may occur at the high flux zone at the coalescence of the western and central subcraters, after vertical flow truncated saturated clay on the floor of the pre-1913 lake (Fig. 11A) and concentrated feeder pathways for fumaroles were subsequently stabilised by mineralisation within vents (Fig. 32). Like the modern eruption craters, subcraters were likely to have hosted lakes following subcrater-forming events, and as such likely deposited low permeability clay beds that may exist today in the subsurface (Fig. 32). During ground deformation, clay seals may be maintained by the clay because of its (very low) plasticity (Table 2).

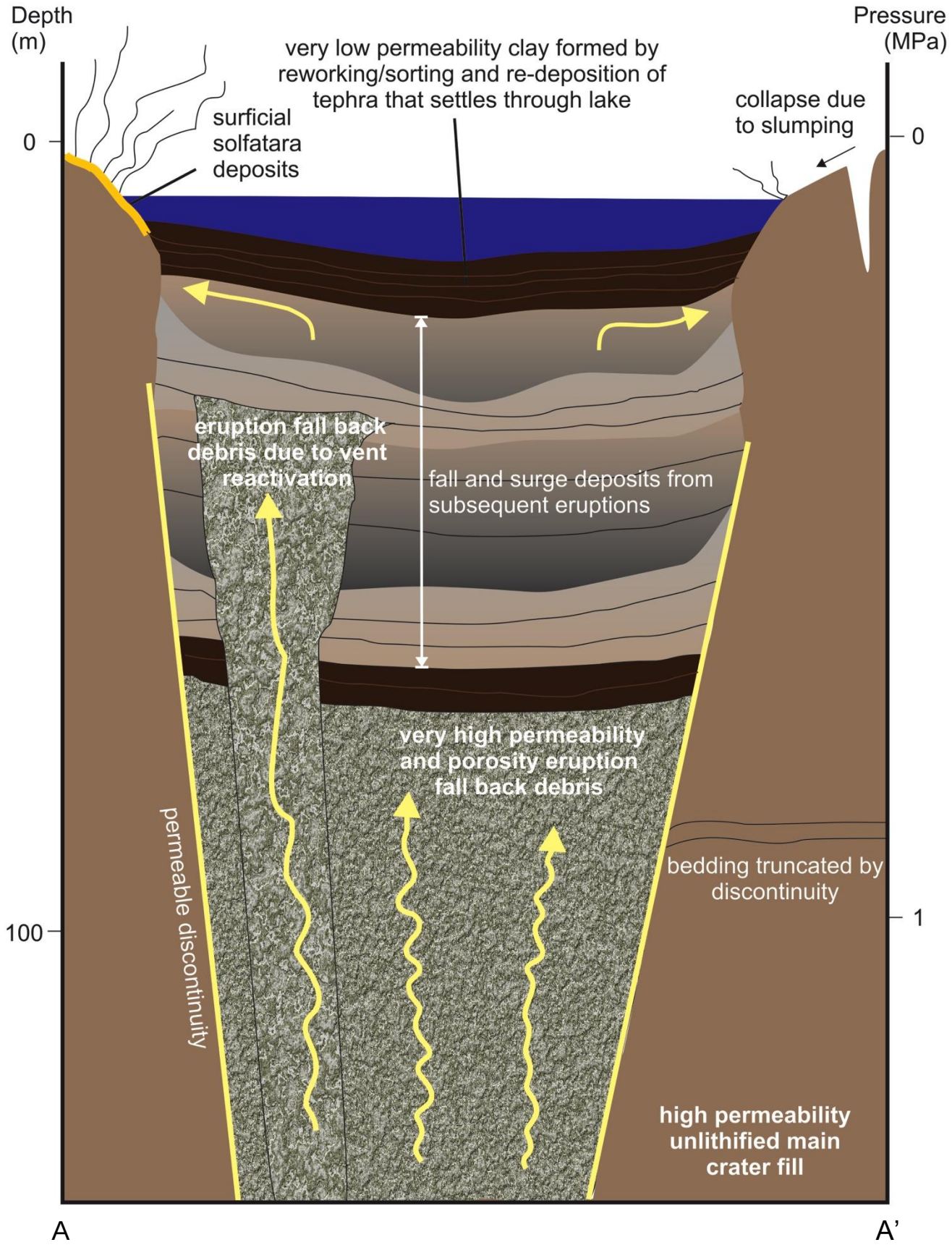

Figure 31 – Schematic 2D model of the structure, lithology, and fluid flow within a typical eruption crater at Whakaari. Based on transect A-A’ in Fig. 12.

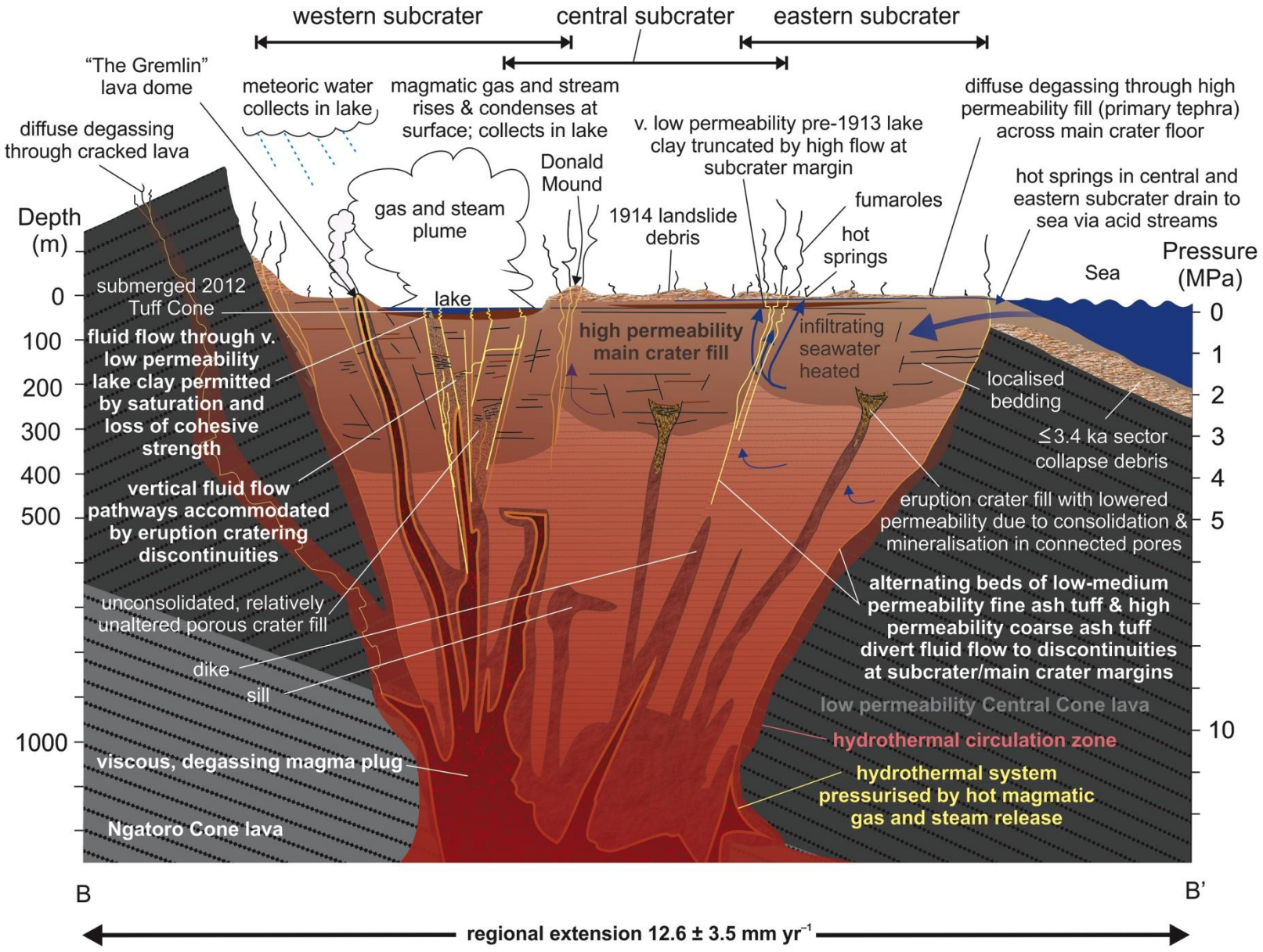

Figure 32 – Schematic 2D model of structure, lithology, and fluid flow in Whakaari's main crater. Based on transect B-B' in Fig. 12. Pressure gradient: Giggenbach et al (2003). Regional extension rate: Lamarche et al (2006).

6.3 Limitations and further research

A key limitation to the proposed model of the ≤3.4 ka sector collapse and occurrence of wet versus dry eruptions is the limited availability of volcanological data (Table 1). Following the eruption of Whakaari's youngest lava flow between 3.4 and 2.6 ka (Cole et al (2000), no eruptions prior to 1826 are known. Field volcanological and stratigraphic analysis for this period is necessary to validate the model by examining the occurrence of phreatomagmatic and (if possible) phreatic eruptions.

An additional limitation of this study is the assumption that fluid flow at Whakaari occurs in either gaseous or liquid state. In reality, Whakaari's fluid flow system features zones of two-state flow where phase changes occur (e.g. boiling of water to vapour) (Giggenbach et al, 2003). Refining the model presented in this study with experimentally determined permeability and strength responses to such behaviour may explain the mechanical processes affecting fluid flow within the sub-surface of the main crater, such as the deformation-related pore pressure increase suggested by Peltier et al (2009) and Fournier & Chardot (2012), or the shallow seismicity recorded by Nishi et al (1996). Furthermore, the results of this study may have implications for other volcanoes worldwide; however such applications were beyond the scope of this study's research plan.

Heat (i.e. high resolution infrared) and mass (i.e. CO_2 soil gas) flux surveys on Whakaari's outer flanks would test the validity of this study's fluid flow model. Areas of particular interest include: (a) the north-eastern flank of the island where Mongillo & Wood (1995)'s infrared survey identified a thermal anomaly at low resolution; (b) the boundary between Central Cone and Ngatoro Cone lava successions (Fig. 12); and (c) Central Cone's main

crater margin and arcuate ring fault (Fig. 12). Results may demonstrate relationships between high permeability and structures related to individual lava flows (Fig. 33), heat released focussed above a dike intrusion, subsurface volcanic cone relationships, and/or magmatic degassing pathways by comparing the results with previously quantified thermal and mass flux (Bloomberg, 2012).

All units measured in this study may exhibit variable permeabilities that affect the proposed fluid flow model (Fig. 32). Further repeated testing of all lithologies would allow sufficient data to investigate the empirical power-law relationship between connected porosity and permeability (as in Klug and Cashman, 1996; Saar and Manga, 1999; Mueller et al, 2005; Mueller et al, 2008). Additionally, representative small-scale cores of breccias could not be made to measure the permeability of talus slopes and collapse debris at Whakaari (e.g. 1914 collapse debris; Fig. 12). This was due to the extremely poorly sorted nature of these deposits, with wide variation in grainsize unable to be contained within a 20 x 40 mm viton jacket. Deposits of the 1914 collapse (Table 1) and smaller landslides (Houghton & Nairn, 1989a; Moon et al, 2009) are thus a component of Whakaari's near-surface and sub-surface geology. Diffuse degassing may occur through breccias in talus slopes at the margin of the main crater (Fig. 33), though it is difficult to assess whether this is due to deep seated structural permeability (i.e. the discontinuities associated with the subcrater margins) or the permeable nature of the talus breccias. It is likely to be a product of both. Similarly, the porosity and permeability of Fe-rich lapilli tuff beds (WI25) are likely to vary due to grain size and sorting variations within beds (Fig. 22) and the porosity and permeability of surficial solfatara deposits are likely to vary due to highly variable and localised sulphur mineralisation (Fig. 23). A representative spread of samples collected from a several different lava flow units identified by Cole et al (2000) may strengthen a correlation to the mass and

flux survey results suggested above for the island's flanks. Further analysis is underway to identify geochemistry of the samples classified in this study (Mayer et al., in prep.).

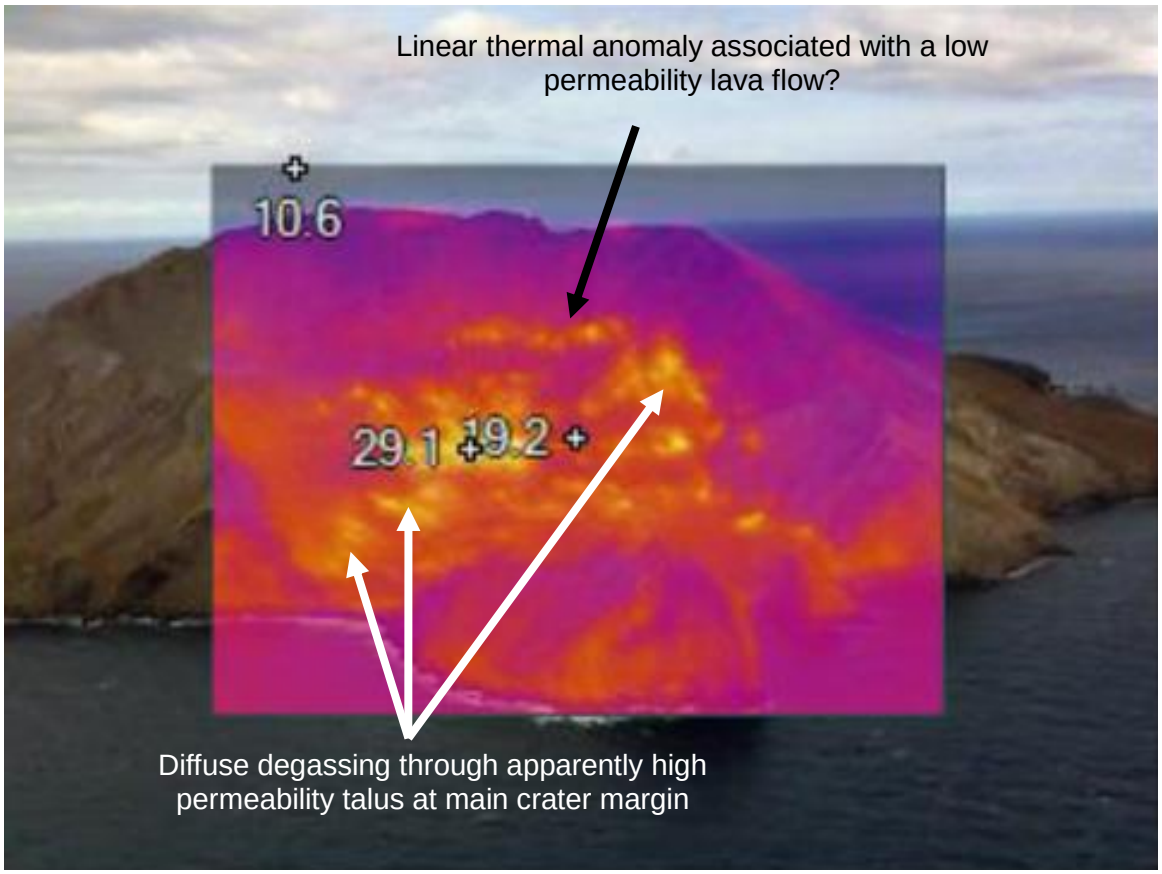

Figure 33 – NW oriented aerial infrared image of Whakaari's crater. Surface temperature values are underestimated but allow relative spatial distribution of thermal areas to be determined. Modified from Dougherty, pers. comm., 2011.

7.0 Conclusions

(1) A prehistoric sector collapse modelled by Moon et al (2009) is inferred to have occurred ≤3.4 ka and was likely to have removed low permeability cone lavas from the eastern section of Whakaari's active Central Cone, allowing a significant increase in lateral seawater infiltration and meteoric water collection above the magma conduit, and possibly increasing the susceptibility to phreatic and phreatomagmatic 'wet' style eruptions.

(2) At Whakaari, low permeability cone lavas and very low permeability reworked tephra/volcaniclastic clay are the two most important lithological constraints on fluid flow in the main crater, whereas unlithified high permeability main crater fill permits diffuse fluid flow and allows seawater and meteoric water infiltration.

(3) Whakaari's recent eruption craters are highly permeable vertical fluid flow pathways. Their permeability decreases due to infilling, consolidation, and mineralisation in pores, and 'capping' by very low permeability clays.

(4) Whakaari's subcrater and eruption crater margins are important structural constraints on fluid flow as they create discontinuities for focussing vertical migration of fluids.

(5) Deposition, consolidation alteration, cementation, alteration, and lithification of main crater deposits are important controls on the spatial and temporal variability of fluid flow within Whakaari's main crater floor.

(6) Representative small-scale gas permeability measurements and geological mapping help to quantify and model geological constraints on fluid flow in active volcanic craters.

8.0 References

Bear, J., (1988), Dynamics of fluids in porous media. Dover Publications, Inc., New York.

Black, P.M., (1970), Observations on White Island Volcano, New Zealand. Bull. Volc. 34(1), 158–167.

Bloomberg S., (2012), Looking for Permeability: Mass and Heat Flow Assessment Using High Resolution soil CO_2 Flux Surveys within the Taupo Volcanic Zone, New Zealand, MSc Thesis, Department of Geological Sciences, University of Canterbury, Christchurch, New Zealand.

Brace, W.F., Walsh, J.B., & Frangos, W.T., (1968), Permeability of granite under high pressure, J. Geophys. Res., 73(6), 2225-2236.

Christoffel, D.A., 1989. Variations in magnetic field intensity at White Island Volcano related to the 1976–82 eruption sequence. In: Houghton, B.F., Nairn, I.A. (Eds.), The 1976–82 Eruption Sequence at White Island Volcano (Whakaari), Bay of Plenty, New Zealand, New Zealand Geological Survey Bulletin, vol. 103. New Zealand Geological Survey, Lower Hutt, 109–118.

Clark, R.H., & Cole, J.W., (1989), Volcanic monitoring and surveillance at White Island before the 1976–82 eruption sequence. In: B.F. Houghton, & I.A. Nairn (Eds.), The 1976–82 eruption sequence at White Island volcano (Whakaari), Bay of Plenty, New Zealand. New Zeal. Geol. Surv. Bull. 103. New Zealand Geological Survey, Lower Hutt, 9 – 12.

Clark, R.H., & Otway, P.M., (1989), Deformation monitoring associated with the 1976–82 White Island eruption sequence. In: Houghton, B.F., & Nairn, I.A. (Eds.), The 1976–82 Eruption Sequence at White Island Volcano (Whakaari), Bay of Plenty, New Zealand, New Zeal. Geol. Surv. Bull. 103. New Zealand Geological Survey, Lower Hutt. 69–84.

Cole J.W., Thordarson, T., & Burt, R.M., (2000), Magma Origin and Evolution of White Island (Whakaari) Volcano, Bay of Plenty, New Zealand. J. Petrol. 41(6), 867-895.

Cole, J.W., & Nairn, I.A., (1975)., Catalogue of the active volcanoes and solfatara fields of New Zealand, Part XXII. In: Decker, R.W. (Ed.), Catalogue of the Active Volcanoes of the World Including Solfatara Fields. International Association of Volcanology and Chemistry of the Earth's Interior, Rome, 38–49.

Cole, J.W., (1990), Structural control and origin of volcanism in the Taupo volcanic zone, New Zealand. Bull. Volcanol., 52, 445-459.

Darcy, H. (1856), De`termination des lois d'e`coulement de l'eau a` travers le sable. Les Fontaines Publiques de la Ville de Dijon. 590–594.

Delmelle, P. & Stix, J. (2000), Volcanic gases. In: Sigurdsson, H. (Edr. In Chf.) (2000) Encyclopedia of Volcanoes. 1st Ed. Academic Press, San Diego. 803-816.

Duncan, A.R., (1970), The petrology and petrochemistry of andesite volcanoes in Eastern Bay of Plenty, New Zealand. PhD. thesis, Victoria University of Wellington, New Zealand.

Forchheimer, P.F. (1901), Wasserbewegung durch Boden, Z. Ver. Deutsch. Ing., 45, 1781-1788.

Fournier N., & Chardot L., (2012), Understanding volcano hydrothermal unrest from geodetic observations: Insights from numerical modelling and application to White Island volcano, New Zealand, J. Geophys. Res., 117(B11208), 1-16.

GeoNet, (2001-13), White Island Volcanic Alert Bulletins. GNS Science, GNS Science Wairakei Research Centre, Taupo.

Giggenbach, W.F., & Glasby, C.P., (1977), Influence of thermal activity on the trace metal distribution in marine sediments around White Island, New Zealand: New Zeal. DSIR Bull., 218, 121–126.

Giggenbach, W.F., (1987), Redox processes governing the chemistry of fumarolic gas discharges from White Island, New Zealand, Appl. Geochem. 2, 143–161.

Giggenbach, W.F., (1995), Variations in the chemical and isotopic composition of fluids discharged from the Taupo Volcanic Zone, New Zealand. J. Volcanol. Geophys. Res. 68(1–3), 89–116.

Giggenbach, W.F., Shinohara, H., Kusakabe, M., & Ohba, T., (2003), Formation of acid volcanic brines through interaction of magmatic gases, seawater, and rock within the White Island volcanic-hydrothermal system, New Zealand, Spec. Publ. Soc. Econ. Geol. 10, 19– 40.

Goff, F., & Janik, C.J. (2000) Geothermal Systems. In: Sigurdsson, H. (Edr. In Chf.) (2000) Encyclopedia of Volcanoes, 1st Ed. Academic Press, San Diego. 817-834.

Hamilton, W.M., & Baumgart, I.L. (Eds.) (1959), White Island. N.Z. Dep. Sci. & Indust. Res. Bull. 127, 9–24.

Holtz, R.D., Kovacs, W.D., & Sheahan, T.C. (2011), An Introduction to Geotechnical Engineering, 2nd Ed. Prentice Hall, New Jersey.

Houghton, B.F., & Nairn, I.A., (1989a), A model for the 1976–82 phreatomagmatic and strombolian eruption sequence at White Island volcano, New Zealand. In: Houghton, B.F., & Nairn, I.A. (Eds.), The 1976–82 Eruption Sequence at White Island Volcano (Whakaari), Bay of Plenty, New Zealand. New Zeal. Geol. Surv. Bull. 103. New Zealand Geological Survey, Lower Hutt. 127–136.

Houghton, B.F., & Nairn, I.A., (1989b), The phreatomagmatic and strombolian eruption events at White Island volcano 1976–82: eruption narrative. In: Houghton, B.F., & Nairn, I.A. (Eds.), The 1976–82 Eruption Sequence at White Island Volcano (Whakaari), Bay of Plenty, New Zealand. New Zeal. Geol. Surv. Bull. 103. New Zealand Geological Survey, Lower Hutt. 13–23.

Houghton, B.F., & Nairn, I.A., (1991), The 1976–1982 Strombolian and phreatomagmatic eruptions of White Island, New Zealand: eruptive and depositional mechanisms at a ‘wet’ volcano. Bull. Volcanol. 54, 25–49.

Hurst, A.W., Rickerby, P.C., Scott, B.J., & Hashimoto, T., (2004), Magnetic field changes on White Island, New Zealand, and the value of magnetic changes for eruption forecasting. J. Volcanol. Geoth. Res. 136, 53–70.

IBWM, (2006), The International System of Units (SI). International Bureau of Weights and Measures. 8th Ed., Paris.

IGNS (1986-2001), White Island Science Alert Bulletins. Institute of Geological and Nuclear Sciences, New Zealand Geological Survey, Lower Hutt.

Jolly, A.D., L. Chardot, C., Neuberg, J., Fournier, N., Scott, B.J., & Sherburn, M., (2012) High impact mass drops from helicopter: A new active seismic source method applied in an active volcanic setting. Geophys. Res. Lett. 39(L12306). 1–5.

King, H., (2013), Volcanic Explosivity Index (VEI). Retrieved 10 Oct. 2013 from: http://geology.com/stories/13/volcanic-explosivity-index/.

Klinkenberg, L.J. (1941) The permeability of porous media to liquids and gases, Drill. Prod. Prac., American Petroleum Institute, 200–213.

Klug, C., & Cashman, K.V., (1996), Permeability development in vesiculating magmas – implications for fragmentation. Bull Volcanol. 58., 87–100.

Lamarche, G., Barnes, P.M., & Bull, J.M., (2006), Faulting and extension rate over the last 20,000 years in the offshore Whakatane Graben, New Zealand continental shelf. Tectonics, 25, TC4005.

Leonard, G.S., Begg., J.G., Wilson, C.J.N. (Cmplrs.) (2010), Geology of the Rotorua area. Institute of Geological and Nuclear Sciences, 1:250 000 geological map 5. 1 sheet + 102 p. GNS Science, Lower Hutt.

Mongillo, M.A., & Wood, C.P., (1995), Thermal infrared mapping of White Island volcano, New Zealand. J. Volcanol. Geoth. Res. 69, 59–71.

Moon, V., Bradshaw, J., Smith, R., & de Lange, W., (2005), Geotechnical characterization of stratocone crater wall sequences, White Island Volcano, New Zealand. Eng. Geol. 81, 146–178.

Moon, V., J. Bradshaw, J., & de Lange, W. (2009), Geomorphic development of White Island Volcano based on slope stability modelling. Eng. Geol. 104, 16–30.

Mueller, S., Melnik, O., Spieler, O., Scheu, B., & Dingwell, D.B., (2005), Permeability and degassing of dome lavas undergoing rapid decompression: An experimental determination. Bull. Volcanol. 67, 526–538.

Mueller, S., Scheu, B., Spieler, O., & Dingwell, D. B. (2008), Permeability control on magma fragmentation. Geology. 36(5), 399–402.

Nairn, I.A., Houghton, B.F., & Cole, J.W., (1996), Volcanic hazards at White Island. 2nd Ed. Ministry of Civil Defence. Volc. Haz. Info. Ser. 3. 1-25.

Nairn, I.A., Houghton, B.F., (1989), Formation of collapse craters and morphological changes in the main crater of White Island volcano during the 1976–82 eruption sequence. In: Houghton, B.F., Nairn, I.A. (Eds.), The 1976–82 Eruption Sequence at White Island Volcano (Whakaari), Bay of Plenty, New Zealand. New Zeal. Geol. Surv. Bull., 103. New Zealand Geological Survey, Lower Hutt, 25–34.

Newhall, C. G., & Self, S., (1982), The volcanic explosivity index (VEI) an estimate of explosive magnitude for historical volcanism. J. Geophys. Res. 87(C2), 1231–1238.

Nishi, Y., Sherburn, S., Scott, B., & Sugihara, M., (1996), High-frequency earthquakes at White Island volcano, New Zealand: Insights into the shallow structure of a volcano hydrothermal system, J. Volcanol. Geotherm. Res. 72(3–4), 183–197.

Peltier A., Scott, B., & Hurst, T., (2009), Ground deformation patterns at White Island volcano (New Zealand) between 1967 and 2008 deduced from levelling data. J. Volc. Geotherm. Res. 181(3–4), 207-218.

Roche, O., van Wyk de Vries, B., & T.H. Druitt, T.H., (2001), Sub-surface structures and collapse mechanisms of summit pit craters. J. Volcanol. Geotherm. Res. 105, 1-18.

Rose, W. I., Chuan, R.L., Giggenbach, W., Kyle, P.R., & Symonds, R.B. (1986), Rates of sulfur dioxide and particle emissions from White Island volcano, New Zealand, and an estimate of the total flux of major gaseous species. Bull. Volcanol., 48, 181– 188.

Saar, M.O., & Manga, M., (1999). Permeability-porosity relationship in vesicular basalts. Geophys. Res. Lett. 26(1), 111–114.

SANZ, (1986). NZS 4402: Methods of Testing Soils for Civil Engineering Purposes. Standards Association of New Zealand.

Scheidegger, A.E. (1974), The physics of flow through porous media. 3rd Ed. University of Toronto Press, Toronto.

Scott, B.J., & Rosenburg., M. (2007), White Island tour: Products and processes of recent activity. Geol. Soc. NZ. Misc. Pub., 123B.

Smithsonian Institution, (2013), White Island. Volcanoes of the World 4.0: The volcano and eruption database of Smithsonian's Global Volcanism Program. Retrieved 2 Oct. 2013 from: http://www.volcano.si.edu/volcano.cfm?vn=241040.

Sottili, G., Palladino, D.M., Gaeta, M., and Masotta, M., (2011), Origins and energetics of maar volcanoes: Examples from the ultrapotassic Sabatini Volcanic District (Roman Province, Central Italy). Bull. Volcanol. 74, 163–186.

Wardell, L. J., Kyle, P.R., Dunbar, N., & Christenson, B. (2001), White Island volcano, New Zealand: Carbon dioxide and sulfur dioxide emission rates and melt inclusion studies, Chem. Geol., 177(1–2), 187– 200.

Werner, C., Hurst, T., Scott, B., Sherburn, S., Christenson, B.W., Britten, K., Cole-Baker, J., & Mullan, B., (2008), Variability of passive gas emissions, seismicity, and deformation during crater lake growth at White Island Volcano, New Zealand, 2002–2006, J. Geophys. Res. 113, B01204.

Wilson, C. J. N., Houghton, B. F., McWilliams, M. O., Lanphere, M. A., Weaver, S. D. & Briggs, R. M. (1995). Volcanic and structural evolution of Taupo Volcanic Zone, New Zealand: a review. J. Volcanol. Geoth. Res. 68, 1–28.

Wood, C.P., (1994), Mineralogy at the volcano-hydrothermal system interface in andesite volcanoes, New Zealand. Geology 22, 75–78.

Wood., C.P., & Browne, P.R.L., (1996), Chlorine-rich pyrometamorphic magma at White Island volcano, New Zealand. J. Volcanol. Geoth. Res. 72, 21-35.

Wright, I.C., (1992), Shallow structure and active tectonism of an offshore continental spreading system: the Taupo Volcanic Zone, New Zealand. Mar. Geol. 103, 287-309.

Wu, S., & Firoozabadi, A. (2011), Simultaneous increase in gas and liquid relative permeabilities and reduction of high-velocity coefficient from wettability alteration, J. Can. Pet. Technol. 50, 17-23.